

What does perturbative QCD really have to say about neutron stars

Dake Zhou^{1,2,3,4,*}

¹*Department of Physics, University of Washington, Seattle, WA 98195*

²*Institute for Nuclear Theory, University of Washington, Seattle, WA 98195*

³*Department of Physics, University of California Berkeley, Berkeley, CA 94720*

⁴*Department of Physics and Astronomy, Northwestern University, Evanston, IL 60208*

(Dated: August 29, 2024)

The implications of perturbative QCD (pQCD) calculations on neutron stars are carefully examined. While pQCD calculations above baryon chemical potentials $\mu_B \sim 2.4$ GeV demonstrate the potential of ruling out a wide range of neutron star equations of state (EOSs), such constraints only affect the most massive neutron stars in the vicinity of the Tolman-Oppenheimer-Volkoff (TOV) limit, resulting in constraints that are orthogonal to current or expected astrophysical bounds. In the most constraining scenario, pQCD considerations favor low values of the squared speed of sound C_s at high μ_B relevant for the most massive neutron stars, but leave predictions of the radii and tidal deformabilities almost unchanged. Such considerations become irrelevant if the maximum speed of sound squared inside neutron stars does not exceed about $C_{s,\max} \sim 0.5$, or if pQCD breaks down below $\mu_B \simeq 2.9$ GeV. Furthermore, the large pQCD uncertainties preclude any meaningful bounds on the neutron star EOS at the moment. Interestingly, if pQCD predictions for the pressure at around $\mu_B \simeq 2.5$ GeV are refined and found to be low ($\lesssim 1.5$ GeV/fm³), evidence for a soft neutron star inner core EOS in combination with the existence of two-solar-mass pulsars would indicate the presence of color superconductivity beyond neutron star densities. We point out that two-solar-mass pulsars place robust upper bounds on this non-perturbative effect and require the pairing gap to be less than $\Delta_{\text{CFL}} \leq 500$ MeV at $\mu_B \simeq 2.5$ GeV.

I. INTRODUCTION

An *ab initio* QCD-based calculation of dense matter beyond a few times the nuclear saturation density ($n_0 = 0.16$ fm⁻³) relevant for the interior of neutron stars remains challenging. This strongly interacting regime not only precludes perturbative calculations but also discourages applications of lattice methods due to the sign problem [1–3]. Such obstacles have deprived us of a clear understanding of neutron stars even though almost a century has passed since their conception by Landau and by Zwicky and Baade [4].

In contrast to the stagnation in this strongly coupled region, significant progress has been made at the low- and ultra-high-density frontiers. On one hand, for baryon number densities below about $\sim 2n_0$, an effective description based on symmetries of QCD has proven fruitful in predicting the properties of neutron-rich matter. Dubbed chiral effective field theory (χ EFT) [5–12], it allows for and arranges all possible operators respecting chiral symmetry through a power counting scheme [8, 10]. The result is a systematic expansion in nucleon momenta that not only enables calculations of the equations of state but also provides error estimates through order-by-order comparisons [13–18]. For example, the recent next-to-next-to-next leading order (N³LO) calculation reveals that the 1σ uncertainties associated with the pressure of pure neutron matter (PNM) to be $\sim 10\%$ at $n_B = n_0$, and worsen to about 40% at $2n_0$ [18]. On the other hand, at densities above $\sim 30 - 50n_0$, asymptotic freedom of

QCD suggests perturbative treatments become valid and useful. The pioneering work of [19, 20] confirmed that cold quark matter resembles closely to a Fermi gas in this region, and has promoted significant efforts in simplifying and improving calculations for cold and dense QCD [21–25].

Given the scarcity of available information directly related to the phase of matter at supranuclear densities in between, gleaming as many insights as possible from both ends is a desirable undertaking. That high-density pQCD calculations may place limits on NS EOSs through thermodynamic consistency requirements is well-known, and there is only a potential for constraints because the current uncertainties associated with pQCD predictions are simply too large to place meaningful bounds. However, a renewed wave of interest in this topic is recently generated by [26]. That letter along with the subsequent papers [27] including attempts to clarify it [28] implicitly made several yet to be justified assumptions and have led to apparently widespread misunderstandings in the literature.

In this first paper of the series exploring the interplay between high- and low-density theoretical inputs we focus on the implications of pQCD calculations on neutron stars and the underlying EOS. One objective is to clarify the misunderstandings on this subject. Specifically, it will be shown that due to our limited understanding of the QCD phase diagram only one type of the bounds derived from thermodynamic relations may be viewed as a constraint on NS EOSs. Furthermore, while pQCD constraints do demonstrate the potential of ruling out a considerable region in the EOS space, astrophysical observables are barely affected by these high-density inputs, as

* dkzhou@berkeley.edu

bounds from pQCD are mostly orthogonal to those from astrophysics.

The rest of the paper is organized as follows. A simple parameterization of χ EFT EOSs is discussed in section II, and the pQCD EOS for cold quark matter is reviewed in section III. In section IV we review the previously-known model-independent bounds on the pressure that the low- and high-density EOSs must satisfy [29–32]. In section V we apply these bounds and carefully examine the underlying assumptions, the applicable ranges, and their consequences. We conclude and outline future directions in section VI. Throughout the discussion we adopt the natural unit system in which $G = \hbar = c = 1$.

II. NEUTRON STAR EOS

In this section we give an overview of the parameterization of neutron star EOSs used in this work. Details will be reported in [33].

A. parameterizing χ EFT-based EOSs with correlated uncertainties

Recently, refs [18, 34] studied truncation errors of χ EFT based on the assumptions that its predictions for energy per particle admit a polynomial expansion in momenta, and that the unknown coefficients associated with higher order terms are natural in size. Using a Gaussian Process (GP) interpolant the authors inferred the size and characteristic length scales of the inter-density correlations of the polynomial coefficients, and used these to obtain extrapolated truncation errors. The resulting correlated uncertainties are encoded in the covariance matrix $\text{Cov}(E_i, E_j)$ where $E_{i,j}$ are energies per particle at the i th and j th tabulated density points, excluding the rest mass. Although one can reconstruct the GP interpolant reported there and use it to generate EOS samples, this approach may not be easily extended to construct beta-equilibrium EOSs that respect the underlying inter-density correlations.

Here, we present a minimal, faithful parameterization of the χ EFT calculations that captures not only the central values but also the correlated truncation errors. The type of correlation we focus on is the inter-density correlation, as it is the most significant one in our approach to describe the beta-equilibrium neutron-rich matter, to be discussed below. For a discussion on the correlation between pure neutron matter (PNM) and symmetric nuclear matter (SNM) EOSs, see [18, 32]. At the core of this parameterization lies the eigenvalue decomposition (singular value decomposition) of the covariance matrix

$$USU^T = \|\text{Cov}(E_i, E_j)\|. \quad (1)$$

The eigenvectors in U are orthonormal since the covariance is symmetric. In particular, each eigenvector U_i

represents a correlation among different densities of the truncation error, with the 1σ variance given by the square root of its corresponding eigenvalue $\sqrt{\text{diag}(S)_i}$. For both the chiral potentials with 450 MeV and 500 MeV cutoffs reported in [18], the largest (second largest) entry in $\sqrt{\text{diag}(S)}$ accounts for about $\sim 90\%$ (8%) of the variances encoded in the full covariance matrix, suggesting their corresponding eigenvectors, which shall be referred to as the most significant eigenvectors, are adequate for current and future astrophysical applications. This procedure is suitable for both PNM and SNM calculations, and for concreteness we focus on the PNM EOS of the form $E(n_n)$ where n_n is the neutron number density.

The two most significant eigenvectors form a set of orthogonal basis to describe the correlated uncertainties. Denote $E_0(n_n)$ the central values of energy per particle predicted by χ EFT, the proposed parameterization that incorporates correlated uncertainties takes the form

$$\begin{aligned} \widehat{E}(n_n) &= \widehat{E}_0(n_n) + \sum_{i=1}^2 a_i \widehat{E}_i(n_n) + m_n, \\ &\text{with } \widehat{E}_i(n_n) = \sqrt{\text{diag}(S)_i} U_i(n_n). \end{aligned} \quad (2)$$

Above, m_n is the mass of neutron. The variance associated with each eigenvector is absorbed into the definition of basis functions $\widehat{E}_i(n_n)$, so that the (uncorrelated) coefficients a_i are independent identical draws from the standard normal distribution $\mathcal{N}(0, 1)$. This procedure effectively projects out the high-dimensional covariance matrix to a lower dimension subspace spanned by the basis functions $\widehat{E}_{i=1,2}(n_n)$.

These basis functions, along with the central values $E_0(n_n)$, are well-behaved and can be faithfully represented by polynomials. For optimal fittings, polynomials of degree $\gtrsim 5$ are sufficient as the fitted EOS as well as derivatives are stationary with increasing polynomial degrees. This allows us to turn the discrete tabulated EOS from χ EFT calculations to a compact, faithful, and continuous representation eq. 2. The resulting EOSs in this parameterization are shown in fig. 1. The pressure follows from the thermodynamic relation $P = n_n^2(dE/dn_n)$, and the 1σ upper and lower bounds of correlated errors are obtained by setting $a_1 = a_2 = \pm 1$ in eq. 2. For comparison, the uncorrelated 1σ errors obtained by taking the square root of $\text{diag}(\|\text{Cov}(E_i, E_j)\|)$ are shown as the blue band. The importance of inter-density correlations is evident as the boundaries of the blue band underestimate the error in pressure by almost $1/3$ near $n_B = 2n_0$. Inter-density correlations are positive since the energy at a given point is less likely to be low if its neighboring points are predicted to have high energies by the chiral interaction.

We note that the EOS in eq. 2 can be parameterized either against number densities n_n or Fermi momenta k_F . The covariance matrix obtained in [18] in fact involves $E(k_F)$ tabulated on an equally spaced grid in Fermi momenta k_F , as inter-density correlations appear more nat-

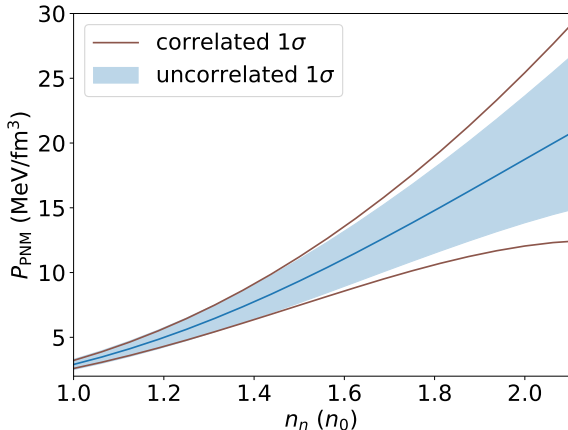


FIG. 1. The pressure of the PNM along with 1σ uncertainties from χ EFT calculations at N3LO. This EOS is based on the chiral potential with a 500 MeV cutoff reported in [18]. The correlated truncation errors are obtained according to eq. 1 and eq. 2, and are shown as the brown lines at the 1σ level. Uncorrelated uncertainties (blue band) underestimate the error in the pressure by as much as 30% near $n_B = 2n_0$, even though it agree with the correlated version on energy per particle within 10% (not shown here).

ural on this grid. It is not straightforward to translate this GP interpolated EOS on the uniform grid of k_F to another GP representation on a grid of different thermodynamic variables, as the physical inter-density correlations are not preserved in the process. This is a limitation due to GP where the kernels are translational invariant. Here, choosing either k_F or n_n is fine since the correlations captured by the basis functions are invariant under change of variables. Interpolation by polynomials does introduce systematics, though a simple estimate by dropping half the points and reproducing them using the remaining data points seems to indicate they are controlled and no more than $\sim 5\%$.

This prescription works well for both PNM and SNM EOSs, but our model focuses on the PNM calculation from [17, 18]. The EOS for nuclear matter in beta-equilibrium is then constructed based on an expansion in proton fraction $x_p = n_p/n_B$ described in [35]. This approach incorporates nuclear saturation properties by imposing a boundary condition at $x_p = 1/2$. Unlike those based on the parabolic expansion centered around $x_p = 1/2$, the resulting beta-equilibrium EOS is only moderately sensitive to the properties of SNM. While theoretical and experimental probes of SNM near and below saturation densities are very valuable inputs, they may suffer from currently unknown systematic uncertainties, as the recent neutron skin measurements might have indicated [36, 37]. Adding that neutron stars are mostly neutrons, we believe this informed yet flexible approach is a noteworthy alternative to those in the literature for connecting nuclear physics to neutron star observables.

For the purpose of this work, the results are insensitive to the choices between SNM-centered or PNM-centered expansions, and we will only present results based on the latter. A systematic comparison of the two and careful examinations of low-energy nuclear inputs will be reported in another work focusing on low-density EOSs.

B. inner core EOS

At higher densities above $n_{\chi\text{EFT}} \simeq 1 - 2n_0$ we adopt two approaches to describe the NS inner core. Firstly, we employ the limiting EOSs that have been long known in the literature. Their predictions in the mass-radius plane encircle all physical possibilities as they yield lower and upper bounds on the pressure at given densities. Due to their ability to delimit the physical regions in the EOS space, they lie at the center of the model-independent framework that propagates the information of cold quark matter at ultra-high densities down below. We will discuss these in detail in section IV. By examining how pQCD calculations impact these extreme scenarios we demonstrate that pQCD cannot improve bounds on NS static observables in section V.

In the second approach, we randomly generate inner core EOSs to explore how pQCD impacts the statistics of NS observables. Since pQCD does not change the boundaries in the mass-radius plane, their impacts on the probabilistic distributions (if and when relevant) would depend upon the assumed NS models. Carefully examining the underlying assumptions in the EOS parameterizations is thus important to ensure robust constraints. We employ a family of speed of sound parameterizations that the author developed in [38] and is perhaps the most agnostic approach in the literature. It has not been published, though a few subsets have been reported elsewhere e.g. [39–41]. We have checked that the results below are robust against different choices of priors on EOS parameters (implicit or explicit), and across different subsets of inner core parameterizations.

III. PERTURBATIVE QCD

At asymptotic densities, QCD becomes perturbative and renders useful an expansion in the strong coupling α_s . The calculation of cold quark matter EOS up to N2LO is first performed in [19, 20] in the momentum space subtraction renormalization scheme, and remains the state-of-art full order calculation. Subsequent works formulated it in the widely adopted $\overline{\text{MS}}$ scheme [22, 42], in which the pressure of unpaired quark matter with $N_f = 3$

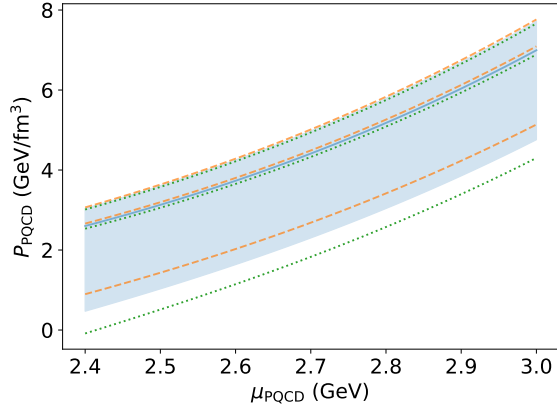


FIG. 2. The pQCD EOS up to N2LO. The blue band shows the renormalization scale uncertainties assuming $\alpha_s(2 \text{ GeV}) = 0.2994$, where the lower boundary corresponds to $X = 1$, the upper boundary corresponds to $X = 4$, and the blue solid line in between to $X = 2$. The green (orange) lines mark the same ranges for $X = [1, 2, 4]$, but assume the 0.5σ upper (lower) bound of $\alpha_s(2 \text{ GeV})$ (see appendix A).

massless flavors is given by

$$P = N_f \frac{(\mu_B/3)^4}{12\pi^2} \left\{ 1 - \frac{2}{\pi} \alpha_s - \frac{N_f}{\pi^2} \alpha_s^2 \log \alpha_s \right. \\ \left. - \frac{\alpha_s^2}{\pi^2} \left[c_1 + N_f \left(\log \frac{N_f}{\pi} - c_2 \right) + \left(11 - \frac{2}{3} N_f \right) \log X \right] \right. \\ \left. + \mathcal{O}(\alpha_s^3) \right\} \quad (3)$$

Above, $c_1 = 18 - 11 \log 2$, $c_2 = 0.535832 \dots$ are numerical constants. The renormalization scale $\bar{\Lambda}$ is implicit in $\alpha_s \equiv \alpha_s(\bar{\Lambda})$ and is conveniently parameterized in terms of the baryon chemical potential by $X = \bar{\Lambda}/(\mu_B/3)$. Since the quark chemical potential $\mu_q = \mu_B/3$ is the characteristic scale of the system, one might expect a good choice of the renormalization scale to be close to it ($X \sim 1$). In ref [43] the authors compared predictions of eq. 3 to an exactly solvable large N_f limit where X is varied between $1/2$ and 2 . It was found that the large N_f prediction lies somewhere in $X \in [1, 2]$, and is a bit closer to $X = 2$. Based on this observation, as well as empirical evidence from hot pQCD calculations, the dense quark matter community appears to have adopted fiducial values $X = 1, 2, 4$ to estimate the renormalization scale uncertainties [22]. This range is shown in fig. 2 as the blue band.

We note that the appearance of X in eq. 3 is an artifact of the perturbation theory since physical observables shall be independent of it. Once higher order corrections are included, pQCD predictions are expected to show diminished sensitivity towards the renormalization scale, assuming pQCD is converging at given μ_B . In this sense, the uncertainty associated with X is in fact a truncation error of the perturbation series. Efforts estimating the

truncation error based on naturalness considerations are underway and will be reported in future work.

Another often neglected source of uncertainties comes from the running of α_s . In the main text we use the two-loop solution of α_s that is consistent with eq. 3. The uncertainty associated with the inferred value of α_s can have a sizable impact on pQCD predictions. This is shown in fig. 2 as the dashed and dotted lines. The effect is especially prominent towards lower values of X , where a percentage difference in the reference value $\alpha_s(2 \text{ GeV})$ would shift the pressure on the order of $\simeq 20 - 50\%$. Note that we do not claim the choice adopted here is the best. A few other options are discussed in appendix A. We merely point out that the uncertainties associated with α_s have to be properly accounted for before claiming robust constraints, and that extracting α_s in the infrared is inherently challenging. For a recent review see [44].

Recently, partial N3LO contributions are computed in [23, 25, 45, 46] for the soft and mixed gluon sectors by resumming diagrams using EFT techniques [47–49]. The newly obtained contributions are the first two positive terms in the series, and hence predict higher pressure at given chemical potentials. However, if calculations of cold dense QED [50] or hot QCD [51, 52] were to be of any guide, the unknown hard contribution at N3LO is likely negative, and the net contribution at full order N3LO may drive the pressure even lower than that of eq. 3. In light of this, we take the cautious approach and employ the N2LO quark matter EOS in the main text. We comment on the impact of the soft contribution at N3LO and present the results in appendix B.

IV. THE LIMITING EOSs AND BOUNDS ON THE PRESSURE

In this section, we review the consistency requirement on low- and high-density EOSs at zero-temperature implied by the limiting scenarios well-known in the literature [29–32]. These extreme scenarios are simply consequences of causality and stability of dense matter, and are often colloquially referred to as the maximally stiff and maximally soft EOSs. They respectively yield the highest (lowest) and the lowest (highest) increments in pressure over arbitrary intervals in chemical potential (density). Since the baryon chemical potential μ_B is the natural parameter in pQCD calculations, we will present them in terms of μ_B in a pedagogical approach.

In the $\mu_B - P$ plane, the pressure P as a function of the baryon chemical potential μ_B must be continuous and differentiable. Furthermore, $P(\mu_B)$ is a convex function since

$$dP/d\mu_B = n_B, \quad (4)$$

$$\frac{d \log n_B}{d \log \mu_B} = C_s^{-1}, \quad 0 \leq C_s \leq 1. \quad (5)$$

where C_s is the speed of sound squared, a non-negative quantity for stable phases. Causality also imposes the

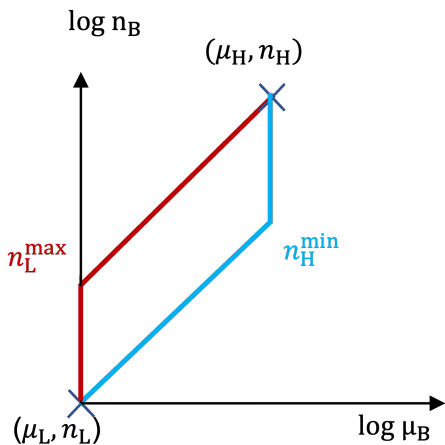


FIG. 3. The maximally stiff (blue) and maximally soft (red) EOSs between μ_L and μ_H that yield ΔP_{\min} and ΔP_{\max} .

additional requirement that $C_s \leq 1$. Together these relations suggest that for a given interval $\Delta\mu_B = \mu_H - \mu_L$ between two arbitrary points which we label “L” and “H”, there exists an upper and a lower bound on $\Delta P = P_H - P_L$, where $P_H = P(\mu_H)$ and $P_L = P(\mu_L)$.

To obtain the upper bound on ΔP , we would like to have the largest possible derivative $\frac{dP}{d\mu_B} = n_B$ throughout the range $[\mu_L, \mu_H]$. The schematics for the limiting cases of $n_B(\mu_B)$ is shown in fig. 3. At μ_L , in order to get the largest value of the number density, we introduce a first order phase transition which can raise n_B by an arbitrary amount at the expense of zero increase in μ_B . But since the slope in the $\log n_B - \log \mu_B$ plane is the inverse of the speed of sound squared, which must be no less than 1 as demanded by causality, jumps in the number density that are too large would overshoot n_H at μ_H . To find the maximum of this value of n_L we start from (μ_H, n_H) and follows the line with the least possible slope $C_s^{-1} = 1$ down to μ_L , where it gives

$$n_L^{\max} = n_H \exp \left[\int_{\log \mu_H}^{\log \mu_L} d \log \mu_B \right] = n_H \frac{\mu_L}{\mu_H}. \quad (6)$$

This point is labeled in red in fig. 3. From there, the EOS we just followed from n_H downwards is the only allowed path to reach (μ_H, n_H) without violating causality $C_s \leq 1$. In fact, this EOS predicts the largest possible number densities between μ_L and μ_H . Therefore, this construction shown in red in fig. 3 leads to the largest possible ΔP given by

$$\Delta P_{\max} = \frac{n_H}{\mu_H} \int_{\mu_L}^{\mu_H} d\mu_B \mu_B = \frac{n_H \mu_H}{2} \left[1 - \left(\frac{\mu_L}{\mu_H} \right)^2 \right].$$

Following similar arguments one finds that the EOS depicted in blue in fig. 3 bears the lowest number densities between μ_L and μ_H . It starts at μ_L with a constant

$C_s = 1$ and reaches μ_H with a number density

$$n_H^{\min} = n_L \exp \left[\int_{\log \mu_L}^{\log \mu_H} d \log \mu_B \right] = n_L \frac{\mu_H}{\mu_L}, \quad (7)$$

then climbs to n_H via a first order phase transition. The resulting lower bound on ΔP reads

$$\Delta P_{\min} = \frac{n_L}{\mu_L} \int_{\mu_L}^{\mu_H} d\mu_B \mu_B = \frac{n_L \mu_L}{2} \left[\left(\frac{\mu_H}{\mu_L} \right)^2 - 1 \right].$$

The constructions shown in red and blue in fig. 3 that give ΔP_{\max} and ΔP_{\min} are commonly referred to as the maximally soft and maximally stiff EOSs in the literature [29–32]. When expressed in terms of number densities, which is useful for describing NS inner cores, they are specified by

$$C_s(n_B) = \begin{cases} 0, & n_B \leq n_L + \Delta n_{\text{PT}} \\ 1, & n_B > n_L + \Delta n_{\text{PT}} \end{cases} \quad \text{maximally soft,} \quad (8)$$

$$C_s(n_B) = \begin{cases} 1, & n_B \leq n_L + \Delta n_{\text{onset}} \\ 0, & n_B > n_L + \Delta n_{\text{onset}} \end{cases} \quad \text{maximally stiff.} \quad (9)$$

Above, the parameters Δn_{onset} and Δn_{PT} that control the location and strength of phase transitions (the segment with $C_s = 0$) are determined by the EOS at the endpoints, and we have just computed them indirectly in eqs. 6 and 7. When the maximally stiff and soft constructions are used to bound NS masses and sizes, these parameters are fixed by the NS maximum mass, also known as the TOV limit M_{TOV} [53, 54]. For specified M_{TOV} , the maximally stiff (soft) construction leads to the largest (smallest) radii at any given $M \leq M_{\text{TOV}}$.

To understand how ΔP_{\min} and ΔP_{\max} impose consistency requirements on the low-density endpoint when the high-density EOS at H is known, we consider two opposite scenarios in which they separately obtain. For low-density EOSs that are soft, i.e., predict high values of P_L at given μ_L , stiff EOSs in the region between μ_L and μ_H are needed to reach the given high-density point specified by (μ_H, n_H, p_H) . If however the low-density EOS is way too soft such that $\Delta P = P_H - P_L < \Delta P_{\min}$, even the maximally stiff EOS between μ_L and μ_H would overshoot p_H at μ_H , suggesting a lack of causal and stable connections between the endpoints. Likewise, in the opposite limit, if the low-density EOS is too stiff predicting pressures that are hopelessly low, even the maximally soft EOS in the region $[\mu_L, \mu_H]$ (which yields ΔP_{\max}) is unable to bring the pressure to P_H at μ_H . Thus, for a given-high density endpoint H , ΔP_{\min} and ΔP_{\max} can in principle rule out low-density endpoints that are inconsistent with thermodynamics and requires

$$\Delta P_{\min} \leq \Delta P \equiv P_H - P_L \leq \Delta P_{\max}$$

without explicitly parameterizing the EOS over the range $[\mu_L, \mu_H]$.

Below, we will take the pQCD predictions at $\mu_{\text{pQCD}} \equiv \mu_H \sim 2.5\text{--}3\text{ GeV}$ as the high-density boundary condition and study the implications of ΔP_{max} and ΔP_{min}

$$\Delta P_{\text{max}} = \frac{n_{\text{pQCD}} \mu_{\text{pQCD}}}{2} \left[1 - \left(\frac{\mu_L}{\mu_{\text{pQCD}}} \right)^2 \right], \quad (10)$$

$$\Delta P_{\text{min}} = \frac{n_L \mu_L}{2} \left[\left(\frac{\mu_{\text{pQCD}}}{\mu_L} \right)^2 - 1 \right], \quad (11)$$

on neutron stars. While in principle both eqs. 10 and 11 can incorporate perturbative information about the cold quark matter at $n_B \sim 30\text{--}50n_0$ to put limits on the NS EOS at lower densities, we shall demonstrate that only eq. 10 can be robustly considered as a constraint, given our current understanding of the zero-temperature QCD phase diagram.

V. IMPLICATIONS FOR NEUTRON STARS

Because of the large separation in density scales between the perturbative regime where pQCD is applicable and the strongly-interacting phase relevant for the interior of neutron stars, it is conceivable that pQCD may only impact (if at all) rather extreme NS EOSs that predict high densities in NSs. We shall show that such speculations are largely correct given the existence of two-solar-mass pulsars, but will clarify the context and criterion for the notion of “closeness”. We will also point out a necessary condition underlying all NS EOSs that are “close enough” to pQCD for which the latter could be relevant. Since the central density of the most massive neutron star is the highest realized in nature thus closest to that of pQCD, we shall always attempt the matching of NS EOS to pQCD via eqs. 10 and 11 at this density to maximize the constraining potentials, though occasionally matching at lower densities will be carried out for clarification purposes. For clarity, we will colloquially refer to the NS EOS at the center of maximum-mass stars as the TOV point.

Refs [26, 27] appear to be the first to report pQCD constraints on the NS EOS through eqs. 10 and 11. The authors chose a few benchmark values of $n_L \sim 4\text{--}8n_0$ as the low-density matching point. Ref [28] pointed out matching at the TOV point is a better choice since the segment above it is not directly probed by NSs. Below, we will highlight the need to choose the EOS-dependent n_{TOV} and μ_{TOV} , the number density and baryon chemical potential at the center of maximum-mass stars, as the low-density matching point, because they correlate with NS observables especially M_{TOV} . Properly taking into account these correlations is crucial to minimize assumptions about the ultra-dense matter not realized in nature.

Astrophysical observations of NSs have already provide valuable insights into the EOS and need to be incorporated to describe realistic neutron stars. In the main text, we will only explicitly take into account the existence of two-solar-mass NSs [55–59], because (1) these measurements are accurate and robust as they exploit relatively clean systems and make minimal assumptions (2) their implied limits on M_{TOV} can be translated to bounds on the NS EOS and NS radii through the maximally stiff and maximally soft EOSs, e.g. [32, 60]. Since potential pQCD constraints on NSs via ΔP_{min} and ΔP_{max} directly act upon the EOS space, this second benefit allows us to obtain model-independent bounds on NS static observables from pQCD. Temporarily deferring astrophysical inputs on the NS radius R and deformability Λ also enables us to isolate the impact of high-density inputs, which helps elucidate the extent and strength of possible constraints on NSs coming from pQCD. We shall show in the main text that pQCD cannot appreciably affect NS global observables such as the radius and the tidal deformability before any astrophysical constraints on these observables are imposed, though it does have the potential of ruling out a considerable number of NS EOSs. In appendix C we demonstrate our results remain valid when astrophysical bounds on R and Λ are taken into account.

The implications of ΔP_{max} and ΔP_{min} will be discussed separately due to their distinct dependencies on the endpoints and different sensitivities towards non-perturbative effects. As mentioned in section II, we employ our χEFT -based EOS up to $n_{\chi\text{EFT}} \sim 1\text{--}2n_0$, where we switch to either (1) the maximally stiff and soft inner cores to obtain bounds on NS observables; or (2) randomly generated inner cores to examine the statistics.

A. ΔP_{min} is not a bound on NSs (yet)

We begin by discussing the implications of ΔP_{min} . For a given low-density matching point μ_{TOV} , n_{TOV} , and P_{TOV} , eq. 11 is solely a function of μ_{pQCD} . It is thus convenient to propagate the information of the TOV point to higher densities by extending the EOS upward using ΔP_{min} . We then compare the extrapolated pressure based on ΔP_{min} to pQCD predictions at μ_{pQCD} in the perturbative regime. This leads to a lower limit on $P_{\text{pQCD}} \equiv P(\mu_{\text{pQCD}})$, requiring that

$$P(\mu_{\text{pQCD}}) \geq P_{\text{TOV}} + \Delta P_{\text{min}}(\mu_{\text{pQCD}}). \quad (12)$$

As explained earlier, violations of eq. 12 would occur if P_{TOV} is too high at μ_{TOV} , so that $P_{\text{TOV}} + \Delta P_{\text{min}}$ overshoots P_{pQCD} at the high-density matching point.

This extension by ΔP_{min} is shown in fig. 4 for the maximally stiff and maximally soft NS EOSs that follow the extremes of 2σ χEFT up to $n_{\chi\text{EFT}} = n_0$ (solid black) and $n_{\chi\text{EFT}} = 2n_0$ (dashed black). The maximally soft NS EOSs are obtained by demanding $M_{\text{TOV}} = 2M_{\odot}$, while for the maximally stiff cases we take $\Delta n_{\text{onset}} \rightarrow \infty$ in eq. 9 (turn off phase transitions) which yield the highest

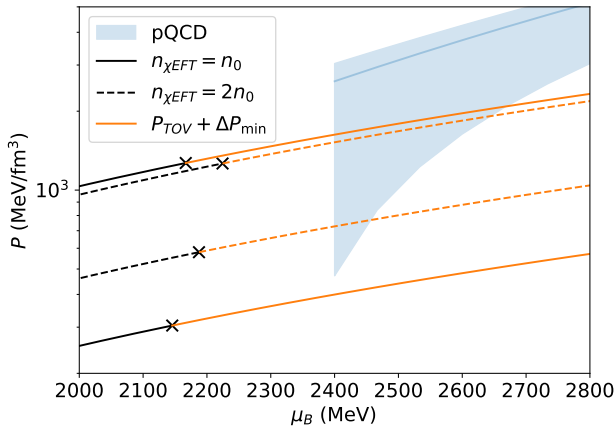


FIG. 4. The ΔP_{\min} bound eq. 12 applied to the maximally stiff and soft NS EOSs. The blue band shows the range of pQCD predictions and is the same as in fig. 2. The solid (dashed) black lines show the limiting NS EOSs based on χ EFT up to $n_{\chi\text{EFT}} = 1.0n_0$ ($2.0n_0$) then switched to the maximally stiff and soft inner cores. They both predict $M_{\text{TOV}} \geq 2.0M_{\odot}$, and are terminated at their respective TOV points marked by the black “x”. From there, they are extended by ΔP_{\min} eq. 11 and yield the right-hand side of eq. 12. These extensions are shown in orange. By the ΔP_{\min} bound eq. 12, any NS EOS whose orange extension lies above the blue curves are incompatible with the underlying pQCD EOS. For the four cases shown, while eq. 12 is always satisfied for pQCD with $X \gtrsim 1.5$, it is violated by those that predict very low P_{pQCD} ($X \simeq 1$). However, this shall not be viewed as a constraint on NS EOSs due to the unknown strengths of non-perturbative effect at μ_{pQCD} not included here.

possible M_{TOV} for given low-density EOS below $n_{\chi\text{EFT}}$. The maximally stiff NS EOSs predict the highest P_{TOV} and are near the bottom of fig. 4, whereas the maximally soft constructions lead to the opposite limit predicting $P_{\text{TOV}} \gtrsim 10^3 \text{ MeV fm}^{-3}$. All four EOSs are truncated at their respective TOV points marked by “x”, where ΔP_{\min} is added and the sum is shown in orange. Equation 12 demands the orange lines to lie below P_{pQCD} (shown in blue) in order that the underlying NS EOSs are consistent with chosen pQCD calculations. For pQCD EOS with $X \gtrsim 2$, P_{pQCD} lie well above the orange curves $P_{\text{TOV}} + \Delta P_{\min}(\mu_{\text{pQCD}})$, suggesting all of the limiting NS EOSs satisfy eq. 12. However, if $X \lesssim 1.5$, soft NS EOSs are in tension with pQCD and appear to be ruled out by eq. 12.

The obvious caveat is that P_{pQCD} currently has considerable uncertainties especially near lower values of X relevant for this constraint. Violations of eq. 12 only occur for pQCD EOSs with $X \lesssim 1.3$, or roughly $P_{\text{pQCD}}(2.4\text{GeV}) \lesssim 1.3 \text{ GeV/fm}^3$. The partial N3LO contribution raises P_{pQCD} and renders this constraint weaker, see fig. 15 in appendix B.

The central issue underlying the above argument is the assumption that the unpaired quark matter described

by pQCD is the true ground state around $\mu_{\text{pQCD}} \simeq 2.5 - 3 \text{ GeV}$. Below $\bar{\Lambda} \sim \mu_q \simeq \text{GeV}$ the strong coupling constant $g_s = \sqrt{4\pi\alpha_s}$ that appears in the Lagrangian is above 1, suggesting non-perturbative effects could still dominate in this regime. Since the determination of ground state requires knowledge of all possible phases we are unable to make the call based on the pQCD EOS alone, even if its uncertainty can be significantly reduced.

In fact, the dense quark matter EOS is known to receive non-perturbative contributions from the pairing of quarks near their Fermi surface. Akin to Cooper pairs in electric superconductors, this gives rise to color superconductivity [61–66] in the cold quark matter (CQM). Assuming the ground state at $\mu_B \gtrsim 2.5 \text{ GeV} \gg 3m_s$ is the most symmetric color-flavor-locked (CFL) superconducting phase, the pressure and density of the CQM are given by

$$\begin{aligned} P_{\text{CQM}} &= P_{\text{pQCD}} + P_{\text{CFL}}, \\ n_{\text{CQM}} &= n_{\text{pQCD}} + n_{\text{CFL}}, \end{aligned} \quad (13)$$

where

$$P_{\text{CFL}} = \frac{\Delta_{\text{CFL}}^2 \mu_B^2}{3\pi^2} \simeq 0.3 \text{ GeV/fm}^3 \left(\frac{\Delta_{\text{CFL}}}{100 \text{ MeV}} \right) \left(\frac{\mu_B}{2.4 \text{ GeV}} \right)^2, \quad (14)$$

$n_{\text{CFL}} = \partial P_{\text{CFL}} / \partial \mu_B$, and Δ_{CFL} is the pairing gap which from the leading order $\mathcal{O}(g_s)$ gap equation is given by $\Delta_{\text{CFL}} / \mu_q \sim \exp(-\text{const}/g_s)$. While estimates based on leading-order pQCD calculations suggest a modest gap $\Delta_{\text{CFL}} \lesssim 10 - 50 \text{ MeV}$ [66], those rooted in phenomenological models reveal much larger possibilities $\Delta_{\text{CFL}} \sim 50 - 200 \text{ MeV}$ at $\mu_B \sim 3 \text{ GeV}$ [65–70]. These values can vary by factors of a few in either direction depending on the color/ flavor/ spin structures of Cooper pairs, higher order corrections, and if non-standard pairings emerge [66].

Taking into account the pairing contribution, the ΔP_{\min} bound eq. 12 should really read

$$P_{\text{pQCD}} + P_{\text{CFL}} \geq P_{\text{TOV}} + \Delta P_{\min}(\mu_{\text{pQCD}}). \quad (15)$$

We see that the tension in fig. 4 goes away if the deficit in P_{pQCD} is compensated by $P_{\text{CFL}} \simeq 600 \text{ MeV fm}^{-3}$ at $\mu_B = 2.4 \text{ GeV}$, which translates to $\Delta_{\text{CFL}} \simeq 200 \text{ MeV}$. When the partial N3LO contribution is included, the deficit in pressure reduces and only requires $\Delta_{\text{CFL}} \simeq 100 \text{ MeV}$, see fig. 14.

The minimum pairing gap $\min\{\Delta_{\text{CFL}}\}$ required to render *any* NS EOS that supports at least $2M_{\odot}$ compatible with pQCD can be found by rearranging eq. 15, which leads to a lower bound on P_{CFL} :

$$\begin{aligned} P_{\text{CFL}}(\mu_B) &\geq P_{\text{TOV}} - P_{\text{pQCD}}(\mu_B) + \Delta P_{\min}(\mu_B) \\ &\equiv \Delta P(\mu_B) + \Delta P_{\min}(\mu_B). \end{aligned} \quad (16)$$

We note that the right-hand side (RHS) of the above inequality has a global maximum across all NS inner core EOSs, and this maximum is reached by the maximally

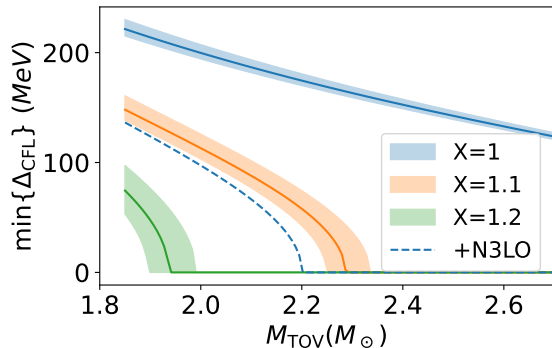


FIG. 5. Lowest superconducting gaps at $\mu_B = 2.4$ GeV required to reconcile tensions with the ΔP_{\min} bound for the maximally soft NS EOSs. These values are robust upper limits on the RHS of eq. 16, assuming χ EFT is valid up to $2n_0$. That is to say, at given M_{TOV} , violations of the ΔP_{\min} bound by *any* NS EOSs can be explained by pairing gaps no greater than the values shown here. The colors represent choices of the pQCD renormalization scale X , and the bands correspond to the 2σ χ EFT uncertainties. The figure is cut off below $M_{\text{TOV}} \leq 1.86M_{\odot}$, the 3σ lower limit of the inferred mass of PSR J0740+6620 [57, 59].

soft NS EOS eq. 8. We show this upper bound in fig. 5 as a function of the NS maximum mass. As noted earlier, violations of ΔP_{\min} may only occur if $X \lesssim 1.2$, and with the partial N3LO contribution included the threshold tightens to $X \lesssim 1.1$ (dashed line). For the N2LO pQCD EOS, gaps less than $\simeq 200$ MeV are adequate to resolve *any* violations of eq. 12 given the existence of two-solar-mass pulsars, and with the N3LO term included, $\Delta_{\text{CFL}} \lesssim 100$ MeV would suffice. It is for this reason we caution that ΔP_{\min} shall not be considered as a bound on the NS EOS until the non-perturbative Δ_{CFL} can be pinpointed exactly.

On the other hand, however, if higher order terms in pQCD narrow down $P_{\text{pQCD}}(2.4 \text{ GeV})$ to be below $\sim 1.3 \text{ GeV}/\text{fm}^3$, astrophysical evidence for a rather soft NS inner core EOS could indicate non-perturbative phenomena around $\mu_B \simeq 2.4 - 3$ GeV. Assuming no additional repulsion is found in the cold quark matter, violations of the ΔP_{\min} bound eq. 12 would strongly support a superconducting gap $\Delta_{\text{CFL}} \simeq 50 - 200$ MeV *above* neutron star densities without directly probing it.

We emphasize that these at-best mild violations of the ΔP_{\min} bound eq. 12 are due to the fact that P_{TOV} is bounded from above. This upper limit is given by the maximally soft NS inner core EOSs. The existence of $2M_{\odot}$ pulsars robustly rules out softer EOSs that predict higher P_{TOV} , e.g., [32]. Had we not taken into account the two-solar-mass pulsars, much stronger violations of ΔP_{\min} would have been allowed and consequently larger minimal superconducting gaps $\min\{\Delta_{\text{CFL}}\}$ required to compensate these deficits. Our model-independent approach utilizing eq. 8 makes this fact explicit and robust.

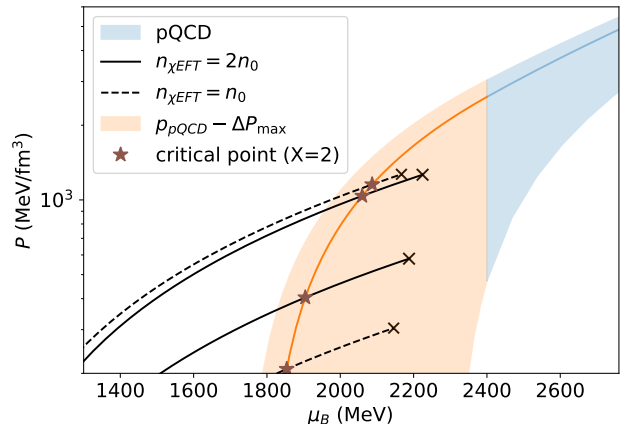


FIG. 6. The ΔP_{\max} bound eq. 17 confronting the maximally stiff and maximally soft NS EOSs. The blue band shows the range of pQCD predictions up to N2LO, and is the same as in fig. 2. The solid (dashed) black lines depict NS EOSs following χ EFT up to $n_{\chi\text{EFT}} = n_0$ ($2n_0$) then switched to the maximally stiff and soft inner cores. They are truncated at their respective TOV points, marked by the black “x”. The RHS of eq. 17 is shown in orange and is matched to pQCD at $\mu_{\text{pQCD}} = 2.4$ GeV. The four limiting NS EOSs are only compatible with eq. 17 if $X \lesssim 1.3$. They are ruled out by a considerable region of the pQCD parameter space at $\mu_{\text{pQCD}} = 2.4$ GeV. The brown stars labeled “critical point” mark the lowest densities at which the bound eq. 17 is violated. Although they lie quite deep inside the TOV points suggesting large sections of the EOSs are ruled out, these excluded segments are only concern stars very close to the TOV limit (see the red segments in fig. 8).

Furthermore, our results are insensitive to astrophysical uncertainties on M_{TOV} . Even if M_{TOV} is at the lower 3σ inferred mass of PSR J0740+6620 $M \approx 1.87M_{\odot}$ [57, 59], the above discussion remains valid (see fig. 5).

B. the ΔP_{\max} bound

For a chosen pQCD EOS at high-density matching point, ΔP_{\max} eq. 10 only depends on μ_L . It is therefore convenient to impose ΔP_{\max} at the high-density endpoint and compare the resulting $P_{\text{pQCD}} - \Delta P_{\max}$ with P_L at the low-density endpoint, requiring

$$P_L \geq P_{\text{pQCD}} - \Delta P_{\max}(\mu_L). \quad (17)$$

As in the previous subsection, we first consider the limiting NS inner core EOSs stitched at either $n_{\chi\text{EFT}} = 2n_0$ (solid in fig. 6) or $n_{\chi\text{EFT}} = n_0$ (dashed). They are shown in black in fig. 6 and are truncated at their respective TOV points. The RHS of eq. 17 is depicted in orange. The bound eq. 17 then rules out any NS EOS that lies above given orange curve, as it is incompatible with the assumed pQCD EOS upon which the ΔP_{\max} extension under consideration is based. It is clear from fig. 6 that

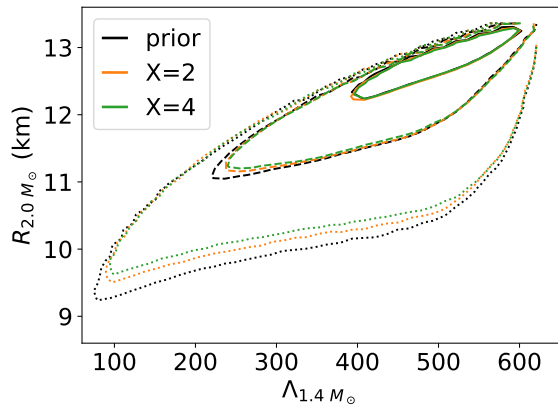


FIG. 7. Confidence intervals (CIs) on $\Lambda_{1.4M_{\odot}}$ and $R_{2.0M_{\odot}}$ before and after imposing the ΔP_{\max} bound at $\mu_{\text{pQCD}} = 2.4$ GeV assuming $X = 2$ (orange) and $X = 4$ (green). The solid, dashed, and dotted lines represent the 50%, 90%, and 99% CIs. The underlying EOS samples follow our χEFT -based low-density model up to $n_{\chi\text{EFT}} = 2n_0$ and are described in section II. Only the existence of two-solar-mass NSs is imposed here. Using the N3LO χEFT EOS [18] up to $n_{\chi\text{EFT}} = 2n_0$ automatically implies $\Lambda_{1.4M_{\odot}} \lesssim 650$ (see also [32]). The posteriors are not appreciably different from the prior, suggesting the ΔP_{\max} constraint is mostly orthogonal to current or expected astrophysical bounds.

all four limiting NS EOSs are in tension with pQCD predictions at $\mu_{\text{pQCD}} = 2.4$ GeV for $X \gtrsim 1.6$. This appears to be quite remarkable since the maximally soft EOSs predict the highest possible pressure P_{TOV} , and yet even these extreme values at around $\mu_B \simeq 2.2$ GeV are still too low to reach the majority of pQCD EOSs at $\mu_B = 2.4$ GeV. On the other end of the spectrum, predictions of P_{TOV} by the maximally stiff NS EOSs are the lowest possible and therefore in stronger tension with a wider range of pQCD calculations. However, owing to the untamed uncertainties associated with P_{pQCD} , even these extremely low values of P_{TOV} cannot be ruled out completely as they are still compatible with eq. 17 when $X \lesssim 1.3$.

Since the maximally stiff and maximally soft inner cores delimit the space of all physical EOSs, it immediately follows that a wide range of NS EOSs may be at risk of being constrained by eq. 17. And for those that are in tension with pQCD, they cannot be ruled out completely because the maximally stiff NS EOSs are yet to be excluded robustly due to the large pQCD truncation errors manifested as a strong sensitivity towards X .

Figure 7 shows predictions for the radius of $2M_{\odot}$ NSs and the tidal deformability of $1.4M_{\odot}$ stars for about 10 million randomly generated samples following χEFT up to $2n_0$. Upon imposing eq. 17 between the EOS-dependent μ_{TOV} and $\mu_{\text{pQCD}} = 2.4$ GeV, about 20%

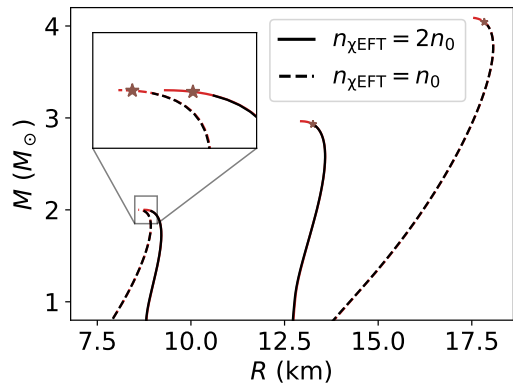


FIG. 8. Mass-radius relations for the maximally stiff and maximally soft NS EOSs. Only the segments shown in red are excluded by the ΔP_{\max} bound imposed at $\mu_B = 2.4$ GeV assuming $X = 4$. The rest of the curves depicted in black are compatible with the chosen pQCD EOS. The onsets of the red segments correspond to the critical points for the underlying NS EOSs, and those assuming $X = 2$ are marked by brown stars as in fig. 6. In any case, no NSs further than $\sim 0.06 M_{\odot}$ away from M_{TOV} are impacted by eq. 17.

of the samples in this pool are excluded¹. We take $X = 2$ and $X = 4$ as they lead to the highest P_{pQCD} and consequently the most optimistic scenario for the ΔP_{\max} constraint. This constraint neither affects appreciably the bounds on $R_{2.0M_{\odot}}$ or $\Lambda_{1.4M_{\odot}}$, nor the correlations between the two observables. While there is a minor preference for slightly higher $R_{2.0M_{\odot}}$ in the posterior, as the excluded samples tend to cluster around the lower end of $R_{2.0M_{\odot}}$ (because the central baryon chemical potentials at $2M_{\odot}$ is further away from that at M_{TOV} for stiffer EOSs, see below), this shift is less than ~ 0.2 km.

To understand better the feeble impacts on NS global observables by the ΔP_{\max} bound eq. 17, let us explicitly examine the segments of NS EOSs affected by eq. 17. We begin by looking at the limiting scenarios shown in fig. 6. As explained earlier, violations of eq. 17 occur when an NS EOS crosses and lies above the chosen orange curve that is specific to a chosen pQCD renormalization scale X . Therefore, for any NS EOS that is in tension with eq. 17, only the segment above the crossing point is excluded. The low-density part preceding the crossing remains valid. We shall refer to these crossings as the “critical” points.

In fig. 6 the critical points of the four limiting NS EOSs are marked by the brown stars assuming $X = 2$. Although significant portions of these EOSs lie above

¹ The fraction of samples excluded by pQCD constraints vary from $\sim 10\%$ to $\sim 60\%$ across different subsets of NS inner core parameterizations, but the effects on observables and EOSs are almost always insensitive to these choices.

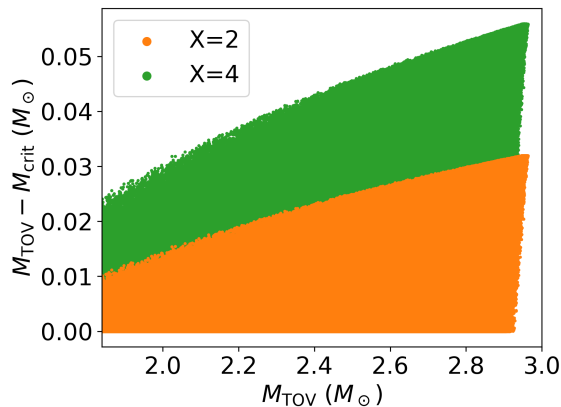


FIG. 9. The distance between M_{crit} and M_{TOV} for samples excluded by eq. 17 in fig. 7. They are also the minimal changes in M_{TOV} needed by the excluded NS EOSs to resolve their tension with eq. 17. These very short distance in NS masses $M_{\text{TOV}} - M_{\text{crit}}$ between the critical point and the TOV point, combined with their considerable separations in baryon chemical potentials $\mu_{\text{TOV}} - \mu_{\text{crit}}$ (see figs. 6 and 11), suggest that sufficiently flexible parameterizations of the NS EOS would not observe noticeable impacts on the size of NSs, since the EOS at TOV points (which eq. 17 directly constrains) would largely decouple from that at much lower μ_B (which astrophysics probes).

the critical point where the baryon chemical potential $\mu_{\text{crit}} \sim 1.8 - 2.0$ GeV, these high-density segments are only probed by stars very close to the maximum mass M_{TOV} . Excluded segments of the mass-radius curves are shown in red in fig. 8. For the maximally soft NS EOSs that support $M_{\text{TOV}} = 2.0M_{\odot}$, the lowest masses impacted by the aforementioned constraint are within $0.01M_{\odot}$ to M_{TOV} . The maximally stiff NS EOSs are more susceptible to such constraints, yet only NSs heavier than about $2.93M_{\odot}$ ($4.04M_{\odot}$) for the one following χEFT up to $n_{\chi\text{EFT}} = 2n_0$ ($n_{\chi\text{EFT}} = n_0$) are affected. Considering their predictions for the maximum mass are $M_{\text{TOV}} = 2.96M_{\odot}$ when $n_{\chi\text{EFT}} = 2n_0$ and $M_{\text{TOV}} = 4.09M_{\odot}$ when $n_{\chi\text{EFT}} = n_0$, it appears unlikely that these minor effects may lead to detectable consequences. Below, for brevity, we shall refer to the lowest NS mass impacted by pQCD via eq. 17 as M_{crit} , i.e., the mass of the star whose central density is the critical point.

The radius of the star at the critical point $R_{\text{crit}} \equiv R(M_{\text{crit}})$ is also very close to R_{TOV} . For the maximally soft NS EOS with $n_{\chi\text{EFT}} = n_0$ ($2n_0$), R_{crit} is about 0.1 km (0.1 km) larger than $R_{\text{TOV}} = 8.6$ km (8.9 km), and for the maximally stiff EOS following χEFT up to n_0 ($2n_0$), R_{crit} is about 0.4 km (0.3 km) larger than $R_{\text{TOV}} = 17.4$ km (12.9 km)². This compounded with nearly flat slopes

dM/dR near the TOV limit strengthens our finding that pQCD is impotent in placing bounds on NS static observables.

Since all possibilities in the mass-radius plane are bracketed by predictions of the limiting NS EOSs³, it is safe to conclude in the absence of additional assumptions that eq. 17 only impacts stars in the vicinity of M_{TOV} . Figure 9 shows the proximity $M_{\text{TOV}} - M_{\text{crit}}$ of critical masses to the TOV limits for excluded samples in fig. 7. For NS EOSs supporting higher M_{TOV} , pQCD constraints radiate further downwards but the effect is confined to a very limited range of NS masses throughout. Indeed, this is a ubiquitous feature shared by every solutions to the TOV equation. For all the EOS samples considered, the derivatives of NS masses with respect to their central baryon chemical potential are small $(dM/d\mu_c)_{2M_{\odot}} \lesssim 10^{-2} M_{\odot}/\text{MeV}$ for two-solar-mass stars and decreases rapidly at higher NS masses.

Our discussion above on the critical points hints at ways of modifying an excluded NS EOS to reconcile it with high-density inputs. Since the segment below μ_{crit} already complies with eq. 17, the minimal modification would be to follow the original EOS up to the critical point, then stick to the ΔP_{max} extension $P(\mu_B) = P_{\text{pQCD}} - \Delta P_{\text{max}}(\mu_B)$ to avoid dropping below it. Implementations of this procedure entail a first order phase transition at μ_{crit} (which gives rise to the sharp corner that bends the $P(\mu)$ curve upwards), followed by a section of constant $C_s = C_{s,\text{max}} = 1$. Notice that this is exactly the scenario depicted in red in fig. 3, and the number density immediately after the phase transition is given by eq. 6. A simple estimate noting that $n_{\text{pQCD}} \simeq 30 - 50n_0$ and $\mu_{\text{crit}}/\mu_{\text{pQCD}} \gtrsim 0.5$ suggests the required jump in densities associated with the first order phase transition is typically huge ($\Delta n_B \gtrsim 10n_0$, $\Delta\mathcal{E} \gtrsim \text{GeV}/\text{fm}^3$, see fig. 19 in appendix D), rendering stable NSs beyond the critical points infeasible. The outcome is an updated TOV limit that sits at $M_{\text{TOV}}^{\text{new}} = M_{\text{crit}}$.

We perform this modification for the excluded samples in fig. 7 and examine their updated predictions for astrophysical observables. As discussed earlier and shown in fig. 9, changes in the maximum mass $\Delta M_{\text{TOV}} = M_{\text{TOV}} - M_{\text{crit}}$ and shifts in the radius of the maximum-mass stars $\Delta R_{\text{TOV}} = R_{\text{TOV}} - R_{\text{crit}}$ are moderate at best. The relative differences $\Delta M_{\text{TOV}}/M_{\text{TOV}}$ and $\Delta R_{\text{TOV}}/R_{\text{TOV}}$ are both less than $\sim 5\%$ for all the samples. Furthermore, neither the central value nor the probability distributions of R_{TOV} are appreciably affected, although those for M_{TOV} are shifted downwards moderately with $\Delta M_{\text{TOV}} \lesssim 0.3M_{\odot}$. This latter effect is prominent for samples predicting $M_{\text{TOV}} \gtrsim 3M_{\odot}$ and can be somewhat sensitive to the priors. But in all scenarios the shift would not exceed $\sim 0.5M_{\odot}$. Therefore, even if

² Predictions of R_{TOV} by the maximally stiff NS EOSs are not a

bound.
³ except for dwarf neutron stars [71].

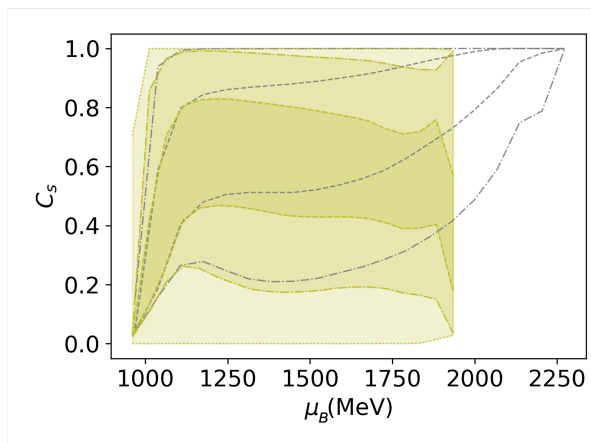


FIG. 10. The prior and posterior of the speed of sound squared C_s for the pQCD constraint in fig. 7. The yellow dashed, dash-dotted, and dotted lines are the 50%, 90%, and 100% posterior CIs respectively, whereas the gray lines show the 50% and 90% priors. The prior appears to be biased toward larger C_s , but this is a consequence of truncating each EOS at its TOV point, and only EOSs with larger C_s predict higher μ_{TOV} (see fig. 11). That the prior is indeed flat is confirmed in fig. 16. This shift in the posterior CIs shown here appears to be the strongest effect eq. 17 could impart to the inference of NS EOSs.

the two-solar-mass pulsars observed so far turn out to be close to the actual TOV limit, pQCD considerations are still unable to affect the inference of their global properties appreciably. This is further confirmed by the probability distributions of both R_{TOV} and R_{2M_\odot} while demanding $M_{\text{TOV}} < 2.3M_\odot$ [55–58], in the absence of this modification. For details see appendix C.

The modifications described above suggest that eq. 17 favors low sound speed near the TOV point. This preference is shown in fig. 10, where posteriors on the squared sound speed C_s are shifted downwards by the aforementioned pQCD constraint, an increasingly noticeable effect towards higher baryon chemical potentials. In appendix C we shall show that this shift is almost orthogonal to constraints expected from astrophysical observations.

It is striking that the pQCD constraint completely rules out $\mu_{\text{TOV}} \gtrsim 1.9$ GeV in the posterior in fig. 10. However, this is not surprising given that even the maximally soft NS EOSs, whose predictions for P_{TOV} are the highest, are excluded in fig. 6 if $X \gtrsim 1.6$. In other words, the bound eq. 17 demonstrates higher sensitivity toward μ_{TOV} over P_{TOV} , in the sense that an NS EOS is more likely in tension with pQCD if it accommodates higher μ_{TOV} , almost independent of its prediction for P_{TOV} , as compared with those predicting lower μ_{TOV} . For example, when matched to pQCD at $\mu_{\text{pQCD}} = 2.4$ GeV, all of the NS EOSs excluded by eq. 17 predict $\mu_{\text{TOV}} \gtrsim 1.8$ GeV. These observations help establish a simple criterion on the applicability of eq. 17. We find that the maxi-

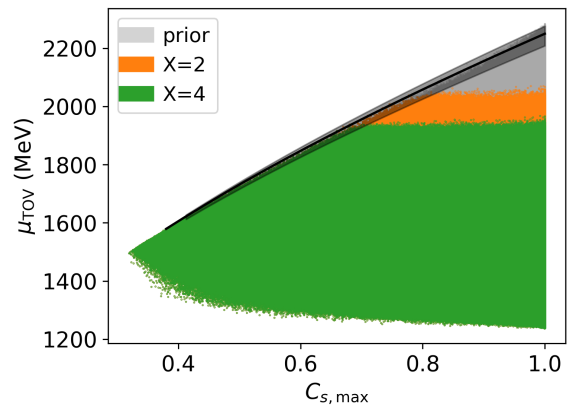


FIG. 11. $C_{s,\text{max}} \gtrsim 0.6$ inside NSs is a necessary condition for NS EOSs constrained by the ΔP_{max} consideration. The collection of EOS samples is shown in gray. The black curve is based on the maximally soft NS EOSs and yield the highest possible μ_{TOV} at fixed $C_{s,\text{max}}$. Its surrounding bands reflect the $\pm 2\sigma$ χEFT uncertainties. Upon imposing the ΔP_{max} bound at $\mu_{\text{pQCD}} = 2.4$ GeV the posteriors for $X = 2$ and $X = 4$ are shown in orange and green respectively. All of the excluded samples predict $\mu_{\text{TOV}} \gtrsim 1.8$ GeV, requiring $C_{s,\text{max}} \gtrsim 0.6$ inside NSs.

imum speed of sound squared $C_{s,\text{max}}$ of an NS EOS informs μ_{TOV} . Assuming χEFT is valid up to $n_{\chi\text{EFT}} = n_0$ ($2n_0$), $C_{s,\text{max}}$ needs to exceed ~ 0.5 (0.6) in order that $\mu_{\text{TOV}} \gtrsim 1.8$ GeV. This correlation also explains the seemingly biased sample selections shown in fig. 10: the prior on C_s favors higher C_s with increasing μ_B because only EOSs with larger $C_{s,\text{max}}$ would lead to higher μ_{TOV} , and if the EOSs are not truncated at their respective TOV points the prior would be mostly flat and featureless. The CIs plotted against number densities shown in fig. 16 also corroborate this.

We plot the correlation between $C_{s,\text{max}}$ and μ_{TOV} in fig. 11. For the strongest constraint with $X = 4$ (green), eq. 17 becomes relevant starting at $\mu_{\text{TOV}} \gtrsim 1.8$ GeV (see also fig. 6), and rules out all NS EOSs with $\mu_{\text{TOV}} \gtrsim 1.9$ GeV. For given $C_{s,\text{max}}$, the maximally soft NS EOSs shown as the black curves give the upper bound on μ_{TOV} where the bands correspond to the 2σ χEFT uncertainties. They reach $\mu_{\text{TOV}} = 1.8$ GeV at around $C_{s,\text{max}} = 0.6$ thus set a lower bound on $C_{s,\text{max}}$ required for any EOS to be “close enough” to pQCD densities. The upshot is that an NS EOS cannot violate eq. 17 unless $C_{s,\text{max}} \gtrsim 0.6$ inside NSs. We note that this is only a necessary condition, and that $C_{s,\text{max}} \gtrsim 0.6$ does not automatically lead to the violation of eq. 17.

Up until now, we have focused on the most optimistic scenarios where the matching to pQCD is performed at $\mu_{\text{pQCD}} = 2.4$ GeV, and have chosen $X = 4$ which yields the highest pressure P_{pQCD} . The constraints weaken drastically if the matching point is raised to

higher baryon chemical potentials. For eq. 17 imposed at $\mu_{\text{pQCD}} = 2.6$ GeV, only NS EOSs with $C_{s,\text{max}} \gtrsim 0.75$ can potentially be ruled out, a condition tightens to $C_{s,\text{max}} \gtrsim 0.9$ for matching at $\mu_{\text{pQCD}} = 2.8$ GeV. If pQCD is imposed above $\mu_B \sim 2.9$ GeV, eq. 17 becomes completely irrelevant. Furthermore, lowering the renormalization scale X also reduces the strength of such constraints. At $X = 1$, no NS EOSs that support $2M_\odot$ can be ruled out, even with soft N3LO contribution to the dense quark matter EOS included.

To account for the pQCD truncation error manifested as dependencies on X , we perform a simple inference by noting that while uncertainties associated with P_{pQCD} are huge, those of the number densities are controlled. We therefore fix n_{pQCD} to the fiducial value $n_B = 5 \text{ fm}^{-3}$, but sample P_{pQCD} randomly from a uniform (and log-uniform) distribution on $[0.5, 3] \text{ GeV/fm}^3$, the approximate range of pQCD predictions at $\mu_{\text{pQCD}} = 2.4$ GeV with $X \in [1, 4]$. Analysis in fig. 10 is then repeated but with this mocked P_{pQCD} data instead. Unsurprisingly, the posteriors on C_s are almost identical to the priors even for $\mu_B \gtrsim 2.0$ GeV, a result independent of values of μ_{pQCD} , whether varying n_{pQCD} , or if the N3LO contributions are included (appendix B)⁴. Since the constraints on $C_s(\mu_B)$ appear to be the strongest, and incorporating uncertainties associated with the running of α_s will further broaden error bands (see appendix A), we believe that meaningful and robust constraints on the NS EOS from pQCD is infeasible at the moment.

We conclude with cautious optimism by providing a forecast on the presumption that P_{pQCD} at $\mu_B = 2.4$ GeV will be reliably and accurately determined. For $P_{\text{pQCD}}(2.4 \text{ GeV}) = 3 \text{ GeV/fm}^3$, the median value of the squared sound speed at the center of maximum-mass stars, $C_{s,\text{TOV}}$, is expected to be lowered by up to 0.2-0.3 by eq. 17, whereas for $P_{\text{pQCD}}(2.4 \text{ GeV}) = 2 \text{ GeV/fm}^3$ the anticipated effect drops to about 0.1-0.2, and would be less than ~ 0.05 if $P_{\text{pQCD}}(2.4 \text{ GeV}) = 1.5 \text{ GeV/fm}^3$ hardly distinguishable from systematic uncertainties due to assumptions in the underlying NS EOSs. Again, these forecasted bounds are almost orthogonal to expected astrophysical constraints, unless highly specific features are assumed for NS EOSs.

C. eq. 17 is the necessary and sufficient condition

As noted above, compliance with eq. 17 at $\mu_L = \mu_{\text{TOV}}$ is the sufficient condition for a given NS EOS, and ensuring it holds for all $\mu_L < \mu_{\text{TOV}}$ is the necessary condition.

⁴ Priors favoring large P_{pQCD} would help, though it is not clear if such choices are justified. We impose priors on P_{pQCD} as it is directly involved in the ΔP_{max} bound. Choosing instead priors on X is also valid but obscures this connection, and the resulting shape of the distribution on P_{pQCD} might not be invariant once higher order terms in pQCD are known.

Hence from a practical point of view, one only needs to check eq. 17 at the TOV point of each NS EOS to determine if the constraint applies. Discussions on the critical point $\mu_{\text{crit}} < \mu_{\text{TOV}}$ only serve to clarify the constraining power of pQCD, and are not necessary in general.

Recently, a so-called integral constraint is proposed in [26]. It is one of several necessary conditions one may conceive. It is equivalent to the one discussed above and is formulated in the $\mu_B - n_B$ plane, although the way it has been applied is only approximate, as the (comparatively controlled and less important for the current purpose) uncertainties associated with χEFT are ignored. Even though this constraint on number density does not reveal new information about NSs beyond what is encoded in eq. 17, for the sake of completeness, we discuss it in appendix D. For a few more useful necessary conditions, see the ensuing letter.

VI. DISCUSSION AND CONCLUSION

Aided by the model-independent bounds on the EOS [29–32, 60], we showed that *ab-initio* cold quark matter calculations in the perturbative regime have the potential of placing robust bounds on the EOS if NSs probe baryon chemical potentials greater than about $\mu_B \sim 1.8 - 2.0$ GeV. The higher the baryon chemical potential realized, the tighter the constraint becomes. If the pressure of NS EOS is too high, the absence of a valid construction between μ_{TOV} and μ_{pQCD} may indicate the presence of non-perturbative effects near $\mu_B \lesssim 3$ GeV. Until the pairing gap can be reliably and accurately calculated, such consideration may not be viewed as a robust constraint on the NS EOS.

On the other hand, an NS EOS may be incompatible with high-density inputs if its prediction for the pressure is too low to reach P_{pQCD} . This is embodied in the ΔP_{max} bound eq. 17, and is the sole requirement an NS EOS needs to comply with currently. Constraints of this type only concern the high-density tails of NS EOSs relevant for stars very close to their respective TOV limits ($M_{\text{TOV}} - M_{\text{crit}}$ no more than $0.06M_\odot$ for $M_{\text{TOV}} = 4M_\odot$, a bound decreases with decreasing M_{TOV}), therefore cannot directly affect observables for most NSs. The strongest constraint possible (at $\mu_{\text{pQCD}} = 2.4$ GeV, assuming $X = 4$ and including the N3LO soft contributions that push P_{pQCD} higher) can at best rule out $R_{\text{TOV}} \lesssim 9.5$ km, or compactness of the maximum-mass stars $C_{\text{TOV}} = M_{\text{TOV}}/R_{\text{TOV}} \gtrsim 0.33$, assuming χEFT is valid up to n_0 . Even if the two-solar-mass pulsars observed to date are in fact the TOV limit, such constraints would only raise the median value of R_{2M_\odot} by no more than 0.2 km. Accounting for the uncertainties of pQCD requires choosing a prior on the renormalization scale X . With natural choices of priors no meaningful bounds can be derived at the moment owing to the wild uncertainties associated with P_{pQCD} .

Although the bound eq. 17 directly applies to the pres-

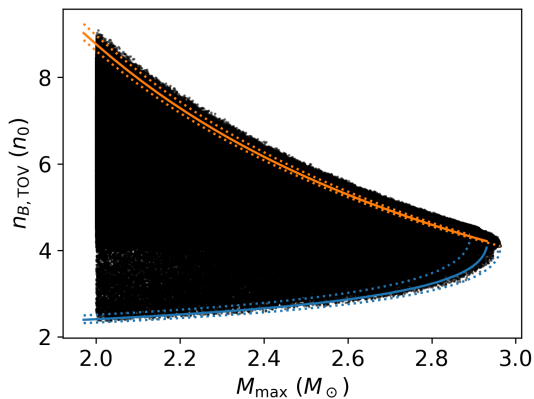


FIG. 12. Correlations between n_{TOV} and M_{TOV} . Stiff NS EOSs supporting high M_{TOV} tend to probe lower densities than those reached by their soft counterparts. The lower bounds are given by the maximally stiff NS EOSs shown in blue. Assuming twin stars are absent, the maximally soft NS EOS shown in orange roughly delimit the upper boundary. The dashed lines indicate the 2σ χ EFT uncertainties.

sure, it is more sensitive to predictions of μ_{TOV} by NS EOSs, as even the highest P_{TOV} by the maximally soft NS EOS at $\mu_{\text{TOV}} \gtrsim 2$ GeV is too low to reach P_{pQCD} for $X \gtrsim 2$ (see fig. 6). Any NS EOS predicting $\mu_{\text{TOV}} \gtrsim 1.8$ GeV is at risk of being ruled out by such considerations. The necessary condition for supporting high values of μ_{TOV} is large $C_{s,\text{max}} \gtrsim 0.6$ inside NSs, see fig. 11.

Unlike the scenarios in section V A, the ΔP_{max} bound in section V B is insensitive to non-perturbative effects. This is because eq. 17 only obtains for high pressure in the quark matter $P_{\text{pQCD}} \gtrsim 2$ GeV/fm³ where contributions from a typical pairing gap $\Delta \sim 200$ MeV $P_{\text{CFL}}/P_{\text{pQCD}} \sim (\Delta_{\text{CFL}}/\mu_q)^2$ would be moderate at best, whereas in section V A only pQCD calculations predicting low pressure are relevant. The ΔP_{max} constraint also appears to be insensitive to the strange quark mass m_s . In the decoupling limit $m_s \rightarrow \infty$, the 2-flavor quark matter EOS only differs by about 20% at $\mu_B \sim 2.6$ GeV, moving the bands in fig. 10 by no more than $\sim 10\%$.

Recently, ref [26] reported another *necessary* condition. As discussed above and detailed in appendix D, this necessary condition does not lead to additional constraints beyond eq. 17. By matching NS EOSs at a fixed density $n_B \sim 5-10n_0$, that letter and the following work [27] excluded a large number of EOSs based on their segments that are not probed by stable NSs. This is especially problematic for stiff NS EOSs as both their predictions for n_{TOV} and for $P(n_B > n_{\text{TOV}})$ are typically low. To illustrate this we show the correlation between M_{TOV} and n_{TOV} in fig. 12. We note that the boundaries in this figure can be reproduced by the maximally stiff (blue) and maximally soft NS EOSs (orange). Failing to account for these correlations would unfairly bias against large values of M_{TOV} . Ref [28] correctly addressed this is-

sue, but arrived at the misleading conclusion that pQCD is not constraining if imposed on top of current astrophysical observations. We clarified that eq. 17 is only relevant for stars very close to the TOV limit so would not affect neutron star observables appreciably, but could yield constraints on the EOS that are mostly orthogonal to astrophysical bounds. Additionally, their claim regarding the possible interplay between pQCD constraints and $R_{2.0M_\odot} \gtrsim 13$ km is likely due to implicit biases in the parameterization of inner core EOSs, which is an approximation to a subset of the ensembles employed in this work. For flexible parameterizations the EOS at the TOV point would largely decouple from that at lower densities, see figs. 6, 8 and 9. Addressing implicit assumptions in the parameterizations of NS EOSs is important and is relevant for a wider range of issues but requires a much lengthier discussion and will be reported in separate work [33]. Finally, we reiterate that eq. 12 cannot be viewed as a constraint on NSs as it is very sensitive to the undetermined strength of the superconducting gap. Given the existence of two-solar-mass pulsars, moderate pairing gaps $\Delta_{\text{CFL}} \lesssim 200$ MeV consistent with current estimates are sufficient to explain any possible violations.

Reducing the uncertainties of the cold quark matter EOS is crucial in materializing the potentials demonstrated in section V B. As noted earlier, although typically referred to as the renormalization scale uncertainties, it is a form of truncation error in disguise, as the dependency on X is an artifact that is expected to receive cancellations when higher order terms are known. This is shown to be the case in dense QED [50] and hot QCD calculations [51, 52], and one could expect it to hold in dense QCD as well assuming pQCD is a valid description down to $\mu_q \sim$ GeV. Effort employing strategies developed in χ EFT [34] to understand better pQCD truncation errors is underway and will be reported in future work.

This work largely confirms previous findings that the knowledge of neutron star global properties alone may not be adequate to distinguish the relevant microscopic degrees of freedom inside the cores of NSs [72]. Although pQCD EOSs predicting high pressure can place upper bounds on the speed of sound above $\mu_B \gtrsim 2$ GeV, we caution against interpreting this as evidence for quark matter, as extrapolating C_s from pQCD predictions above $\mu_B \sim 2.5$ GeV to the strongly-interacting phase at such low densities may be unwarranted. Understanding the phase of matter in this intermediate density range is inherently challenging as neither pQCD nor NSs directly probe this regime. The ensuing letters in this series aim to fill this gap and report model-independent studies on the ultra-dense matter.

Very recently, ref [73] performed a Bayesian analysis based on parameterizing the NS EOS to infer upper bounds on the superconducting gap. We wish to point out that this constraint can be obtained model-independently with the help of maximally soft NS EOSs,

see appendix E.

Appendix A: the running of α_s

ACKNOWLEDGMENT

I would like to thank Sanjay Reddy for discussions. During the conception and completion of this work the author is supported by Grant No. PHY-1430152 (JINA Center for the Evolution of the Elements) and the Institute for Nuclear Theory Grant No. DE-FG02-00ER41132 from the Department of Energy, and by NSF PFC 2020275 (Network for Neutrinos, Nuclear Astrophysics, and Symmetries (N3AS)).

We give a brief overview of the uncertainties associated with $\alpha_s \equiv g_s^2/(4\pi)^2$ around $\sim \text{GeV}$ scales. To obtain the strong coupling constant at a given scale $\bar{\Lambda}$ we solve the renormalization group equation

$$\frac{d\alpha_s}{d \log \bar{\Lambda}^2} = - \sum_{i \geq 0} \frac{\beta_i}{(4\pi)^{i+1}} \alpha_s^{i+2} = - \sum_{i \geq 0} b_i \alpha_s^{i+2} \quad (\text{A1})$$

up to 2, 3, 4 and 5 loops. For $N_c = 3$ QCD with N_f active flavors of quarks the beta function coefficients are given by [74]

$$\beta_0 = 11 - \frac{2N_f}{3}, \quad (\text{A2})$$

$$\beta_1 = 102 - \frac{38N_f}{3}, \quad (\text{A3})$$

$$\beta_2 = \frac{325N_f^2}{54} - \frac{5033N_f}{18} + \frac{2857}{2}, \quad (\text{A4})$$

$$\beta_3 = \frac{149753}{6} + 3564\zeta_3 - \left(\frac{1078361}{162} + \frac{6508}{27}\zeta_3 \right) N_f + \left(\frac{50065}{162} + \frac{6472}{81}\zeta_3 \right) N_f^2 + \frac{1093}{729} N_f^3, \quad (\text{A5})$$

$$\begin{aligned} \beta_4 = & \frac{8157455}{16} + \frac{621885}{2}\zeta_3 - \frac{88209}{2}\zeta_4 - 288090\zeta_5 + \left(-\frac{336460813}{1944} - \frac{4811164}{81}\zeta_3 + \frac{33935}{6}\zeta_4 + \frac{1358995}{27}\zeta_5 \right) N_f \\ & + \left(\frac{25960913}{1944} + \frac{98531}{81}\zeta_3 - \frac{10526}{9}\zeta_4 - \frac{381760}{81}\zeta_5 \right) N_f^2 \\ & + \left(-\frac{630559}{5832} - \frac{48722}{243}\zeta_3 + \frac{1618}{27}\zeta_4 + \frac{460}{9}\zeta_5 \right) N_f^3 + \left(\frac{1205}{2916} - \frac{152}{81}\zeta_3 \right) N_f^4, \end{aligned} \quad (\text{A6})$$

where $\zeta_n \equiv \zeta(n)$ are values of the Riemann zeta function. Coefficients beyond 2 loop (β_1) are renormalization scheme dependent, and the values quoted above are given in $\overline{\text{MS}}$. Equation A1 can be solved either numerically, or analytically albeit approximately in a perturbative fash-

ion. Defining $t = 2 \log(\bar{\Lambda}/\bar{\Lambda}_{\overline{\text{MS}}})$ and $l = \log(t)$, an iterative solution to the 5-loop renormalization group equation ($\mathcal{O}(\alpha_s^6)$ on the right hand side of eq. A1) is given by

$$\begin{aligned} \alpha_s(\bar{\Lambda}^2) = & \frac{1}{b_0 t} \left[1 - \frac{b_1 l}{b_0^2 t} + \frac{b_1^2 (l^2 - l - 1) + b_0 b_2}{b_0^4 t^2} + \frac{b_1^3 (-2l^3 + 5l^2 + 4l - 1) - 6b_0 b_1 b_2 l + b_0^2 b_3}{2b_0^6 t^3} \right. \\ & \left. + \frac{18b_0 b_2 b_1^2 (2l^2 - l - 1) + b_1^4 (6l^4 - 26l^3 - 9l^2 + 24l + 7) + 2b_0^2 (5b_2^2 + b_0 b_4) - b_0^2 b_1 b_3 (12l + 1)}{6b_0^8 t^4} \right]. \end{aligned} \quad (\text{A7})$$

Its exact derivatives up to the second order are

$$\begin{aligned} \frac{d\alpha_s(\bar{\Lambda}^2)}{d \log \bar{\Lambda}^2} = & -\frac{1}{b_0 t^2} \left[1 + \frac{b_1 (1 - 2l)}{b_0^2 t} + \frac{b_1^2 (-2 - 5l + 3l^2) + 3b_0 b_2}{b_0^4 t^2} \right. \\ & + \frac{b_1^3 (-4 + 3l + 13l^2 - 4l^3) + 3b_0 b_2 b_1 (1 - 4l) + 2b_0^2 b_3}{b_0^6 t^3} \\ & \left. + \frac{b_1^4 (11 + 138l + 33l^2 - 154l^3 + 30l^4) + 18b_0 b_2 b_1^2 (-4 - 9l + 10l^2) + b_0^2 b_3 b_1 (7 - 60l) + 10b_0^2 (5b_2^2 + b_0 b_4)}{6b_0^8 t^4} \right], \end{aligned} \quad (\text{A8})$$

$$\frac{d^2\alpha_s(\bar{\Lambda}^2)}{d(\log \bar{\Lambda}^2)^2} = \frac{2}{b_0 t^3} \left[1 + \frac{b_1(5-6l)}{2b_0^2 t} + \frac{b_1^2(-3-26l+12l^2) + 12b_0 b_2}{2b_0^4 t^2} + \frac{-b_1^3(23+11l-77l^2+20l^3) + 3b_0 b_2 b_1(9-20l) + 10b_0^2 b_3}{2b_0^6 t^3} + \frac{3b_0 b_2 b_1^2(60l^2-74l-15) + b_1^4(127l+110l^2-174l^3+30l^4) + b_0^2 b_3 b_1(17-60l) + 10b_0^2(5b_2^2 + b_0 b_4)}{2b_0^8 t^4} \right]. \quad (\text{A9})$$

We do not use the renormalization group equation eq. A1 to compute the derivatives as eq. A7 is only an approximate solution to the 5-loop renormalization group equation. The residue, although small, would spoil the thermodynamic consistency of the pQCD EOS if eq. A1 were to be used in calculating $n_B = \frac{dP}{d\mu_B}$ and $C_s = d \log \mu_B / d \log n_B$.

The 2-, 3-, 4-loop solutions of α_s can be obtained by setting $b_{i>n_{\text{loop}}-1} = 0$ where $n_{\text{loop}} = 2, 3, 4$. It is also customary, although not necessary, to truncate the iterative solutions in eq. A7 at order $\left(\frac{b_i}{b_0^i}\right)^{n_{\text{loop}}-1}$ in the literature, i.e., only keep the leading power in $b_{n_{\text{loop}}-1}$. We also adopt this convention throughout this paper.

The Landau pole $\bar{\Lambda}_{\overline{\text{MS}}}$ is determined once the strong coupling at a given reference scale is specified. Above, we took the value $\alpha_s(\bar{\Lambda} = 2 \text{ GeV}) = 0.2994_{-0.0141}^{+0.0152}$ from the 2008 particle data group (PDG) report. The resulting P_{pQCD} and its uncertainties at $\mu_B = 2.4 \text{ GeV}$ are shown in fig. 13. Since then, PDG only reports $\alpha_s(\bar{\Lambda} = M_Z)$. Running α_s from the Z boson mass $M_Z \sim 100 \text{ GeV}$ to GeV scales is not straightforward as the decoupling of both charm and bottom quarks occurs in this regime. But because the uncertainties of $\alpha_s(M_Z)$ are barely reduced since 2008, we do not expect significant improvements for the bound on $\alpha_s(2 \text{ GeV})$ quoted above. Furthermore, the current inferred values of $\alpha_s(M_Z)$ could suffer from non-negligible modeling uncertainties as a few subsets of measurements behind the PDG averaged value appear to be in disagreement [75]. A careful running of α_s from M_Z where $N_f = 5$ to $\sim \text{GeV}$ scales where $N_f = 3$ will be performed in a future work.

An alternative approach is to take the values of Landau pole $\bar{\Lambda}_{\overline{\text{MS}}}$ reported in the literature. This is generally disfavored as these values can be quite sensitive to the order of renormalization group equations used in the analysis. For instance, in fig. 13 the underlying $\bar{\Lambda}_{\overline{\text{MS}}}$ ranges from ~ 310 to $\sim 390 \text{ MeV}$. In [76] the authors matched lattice data for the static $q\bar{q}$ potential to a resummed next-to-next-to-next-leading log perturbative calculation in the perturbative regime $\sim 5 \text{ GeV}$ and obtained $\bar{\Lambda}_{\overline{\text{MS}}} = 315_{-12}^{+18} \text{ MeV}$. pQCD EOS based on this value is shown as the last column in fig. 13 and is labeled as “lattice”, where we assumed a 4-loop running α_s that is used throughout [76]. It is not clear if some of the choices are better than others.

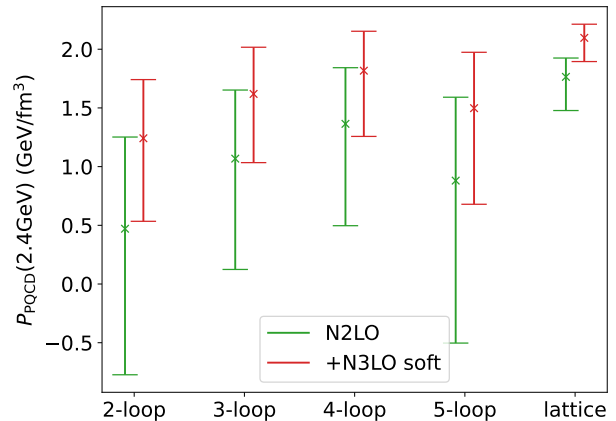


FIG. 13. Pressure of the pQCD EOS with $X = 1$ at $\mu_B = 2.4 \text{ GeV}$ obtained with 2-, 3-, 4-, and 5-loop QCD beta functions. The central values and error bars correspond to those of the reference value $\alpha_s(\bar{\Lambda} = 2 \text{ GeV}) = 0.2994_{-0.0141}^{+0.0152}$. The last column labeled “lattice” uses the extracted Landau pole from lattice data [76] and is obtained with a 4-loop running (see main text). The 2-loop α_s adopted in the main text leads to the largest uncertainties, but is consistent with the N2LO pQCD calculation eq. 3. Notice that the effect of the N3LO soft contribution can be significant, and in most cases appear to improve the convergence of pQCD.

Appendix B: the partial N3LO pQCD EOS

The soft N3LO contribution to the pQCD EOS recently reported in [23, 25] pushes the pressure higher than that predicted by the N2LO result eq. 3, as can be seen in fig. 13. Although this makes eq. 17 more constraining, the main conclusions remain unchanged. For instance, as is shown in fig. 14, the maximally stiff EOSs are still compatible with pQCD predictions assuming $X = 1$. Since the maximally stiff inner core EOS predicts the lowest pressure at $\mu_B \sim 2.2 \text{ GeV}$, no other valid NS EOSs can be ruled out either.

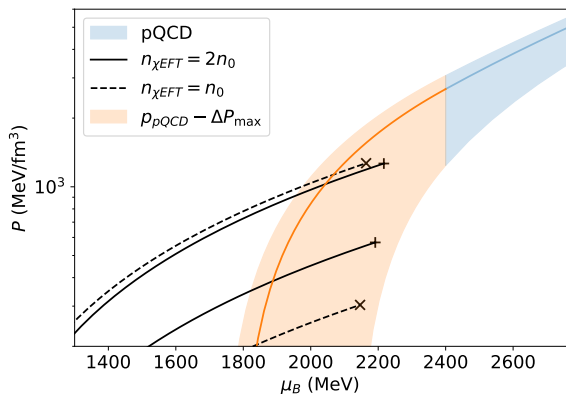


FIG. 14. Similar to fig. 6 except that the partial N3LO contribution is included in the pQCD EOS. None of the NS EOSs are completely ruled out.

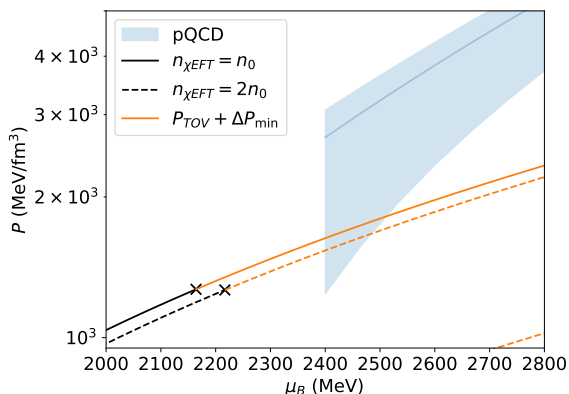


FIG. 15. Similar to fig. 4 except that the partial N3LO contribution is included. The effect of eq. 11 becomes weaker. As explained earlier this is not a constraint on NS EOSs. Since predictions for P_{pQCD} at given X are not expected to be invariant when higher order terms are included in pQCD, and the uncertainties in n_{pQCD} are relatively controlled, it is more convenient to directly parameterize pQCD uncertainties in terms of P_{pQCD} . For instance, if $P_{\text{pQCD}}(2.4\text{GeV}) = 1.2\text{ GeV/fm}^3$ and the maximally soft EOSs are confirmed by astrophysics, assuming the ground state is a CFL phase the pairing gap needs to be at least $\sim 50\text{ MeV}$.

Appendix C: incorporating constraints on NS sizes

We have shown in the main text with both limiting scenarios and with randomly generated samples that (potential) pQCD bounds are orthogonal to those from astrophysical observations. Here we strengthen this statement by explicitly taking into account astrophysical constraints. Specifically, we impose the tentative bounds on the tidal deformability of $1.4M_{\odot}$ stars $\Lambda_{1.4M_{\odot}} \leq 500$ from GW170817 [77–79], and the putative upper limit $M_{\text{TOV}} \lesssim 2.3M_{\odot}$ based on speculations that the remnant of GW170817 collapsed to a black hole within sec-

onds [80, 81]. That the former is orthogonal to pQCD considerations is demonstrated earlier in fig. 7, and that the latter might interfere with pQCD constraints is mainly due to the closer proximity of the TOV limit to $2M_{\odot}$ stars. However, we do not find any appreciable shifts in the observables of $2M_{\odot}$ stars. The same observation holds for the posterior CIs of $C_s(\mu_B)$ (see fig. 17) where the effects of pQCD considerations are perhaps the strongest.

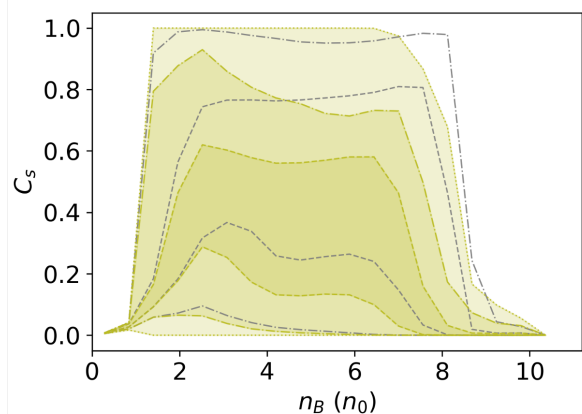


FIG. 16. Similar to fig. 10 except plotted in the $n_B - C_s$ plane. Notice that the prior CIs shown in black are centered around 0.5 and mostly flat, confirming the peculiar shape seen in fig. 10 is a feature of solutions to the TOV equation instead of an indication of bias. Since the pQCD constraint directly impacts $C_s(\mu_B)$, its effects here can be somewhat sensitive to the assumptions underlying the NS EOSs. The results shown here, which drive the CIs lower without introducing additional features, appear to be general and insensitive to those assumptions.

Appendix D: the number density constraint

The low-density matching points in the ΔP_{min} and ΔP_{max} bounds are taken to be at or below the TOV points of NS EOSs, which vary from one EOS to another. The number density constraint derived in [26] is in a sense a global bound that concerns fixed low- and high-density matching points L and H. We will take the low- and high-density matching points to be $\mu_{\chi\text{EFT}}$ and μ_{pQCD} as in [26]. For all EOSs that pass through an arbitrary point (μ_1, n_1) between the two endpoints there exist a maximum and a minimum value of ΔP . These limiting cases are shown as the blue and the red curves in fig. 18. By noting the constructions in the density ranges $[\mu_L, \mu_1]$ and $[\mu_1, \mu_H]$ are two separate realizations of fig. 3, the expressions for ΔP_{min} and ΔP_{max} can be obtained by replacing the dummy labels in eqs. 10 and 11,

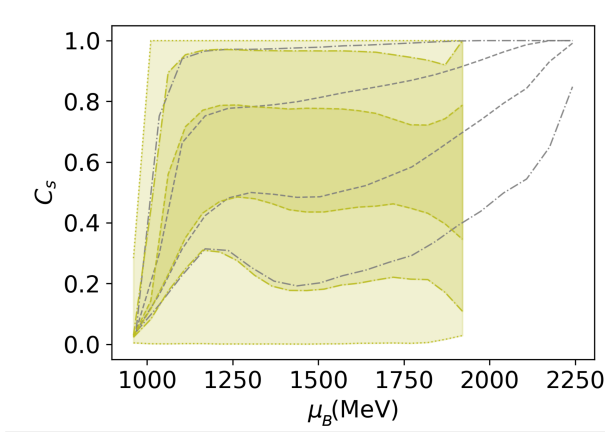


FIG. 17. Similar to fig. 10 but assumes a prior that already incorporates astrophysical constraints $\Lambda_{1.4M_\odot} \leq 500$ and $M_{\text{TOV}} \leq 2.3M_\odot$. When compared to fig. 10 we see that the astrophysical inputs have negligible effects on $C_s(\mu_B)$, even in this hard cutoff approach ignoring astrophysical uncertainties. The pQCD bound once again shifts the CIs on C_s towards lower values, and forbids μ_{TOV} above ~ 1.9 GeV.

and are

$$\Delta P_{\text{max}} = \frac{n_H \mu_H}{2} \left[1 - \left(\frac{\mu_1}{\mu_H} \right)^2 \right] + \frac{n_1 \mu_1}{2} \left[1 - \left(\frac{\mu_L}{\mu_1} \right)^2 \right], \quad (\text{D1})$$

$$\Delta P_{\text{min}} = \frac{n_L \mu_L}{2} \left[\left(\frac{\mu_1}{\mu_L} \right)^2 - 1 \right] + \frac{n_1 \mu_1}{2} \left[\left(\frac{\mu_H}{\mu_1} \right)^2 - 1 \right]. \quad (\text{D2})$$

In order that there exists an EOS passing through (μ_1, n_1) , $\Delta P_0 \equiv P_H - P_L$ has to be sandwiched by these limits $\Delta P_{\text{min}} \leq \Delta P_0 \leq \Delta P_{\text{max}}$. But as discussed earlier, only the ΔP_{max} bound may be used as a constraint, and it leads to the number density constraint $n_1(\mu_1) \geq n_{\text{min}}(\mu_1)$ where

$$n_{\text{min}}(\mu) = \frac{2\Delta P_0 - \mu_H n_H \left[1 - \left(\frac{\mu}{\mu_H} \right)^2 \right]}{\mu \left[1 - \left(\frac{\mu_L}{\mu} \right)^2 \right]}. \quad (\text{D3})$$

This lower limit can be relevant for large μ close to μ_H , but it blows off near μ_L . In fact, it crosses the lower bound eq. 7 (noting that ‘H’ and ‘L’ are just dummy labels there) set by the maximally stiff EOS (blue curve in fig. 18) at

$$\mu_C = \sqrt{\frac{\mu_L \mu_H (\mu_L n_L - \mu_H n_H + 2\Delta P_0)}{\mu_H n_L - \mu_L n_H}}. \quad (\text{D4})$$

Therefore, for baryon chemical potentials below this value μ_C , eq. 7

$$n_{\text{min}}(\mu) = \frac{\mu}{\mu_L} n_L \quad (\text{D5})$$

is the relevant bound.

The n_{min} bound is shown in fig. 19 as the dashed, dot-dashed, and dotted lines for $X = 1, 2, 4$. The high-density pQCD point is taken to be $\mu_H = 2.4$ GeV, and we have included the pQCD N3LO leading log term. To compare this necessary condition with the one from eq. 17, we show a few modified NS EOSs described in the main text as solid lines. These are based on the maximally stiff and maximally soft EOSs in fig. 6, and are diverted away at the critical points just before eq. 17 is violated via first-order-phase transitions. These two approaches lead to the same constraint. This equivalence can be understood by noting that ΔP_{max} does not depend on n_L , and the maximally stiff (soft) EOS depicted in blue (red) between μ_L and μ_1 is, plainly, the maximally stiff (soft) inner core EOS shown in fig. 19. In other words, any causal and stable NS EOS will automatically satisfy the contributions to ΔP_{max} below μ_1 . This effectively reduces the problem formulated on the interval $[\mu_L, \mu_H]$ to that on $[\mu_1, \mu_H]$, which is exactly fig. 3.

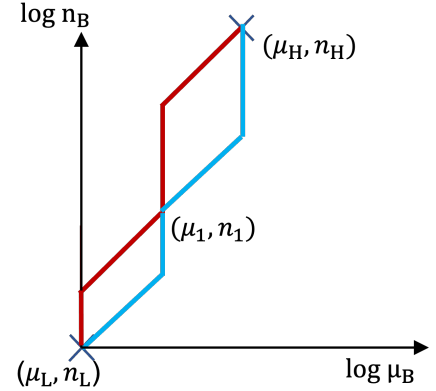


FIG. 18. Schematics for the number density constraint for fixed endpoints and $\Delta P_0 = P(\mu_H) - P(\mu_L)$. The curve in blue (red) yields ΔP_{min} (ΔP_{max}) among all possibilities that pass through the point (μ_1, n_1) . These constructions are obtained by stacking two copies of fig. 3 on top of each other.

For the sake of completeness, we also provide the expression for n_{max} derived from $\Delta P_{\text{min}} \leq \Delta P_0$:

$$n_{\text{max}}(\mu) = \frac{2\Delta P_0 - \mu_L n_L \left[\left(\frac{\mu}{\mu_L} \right)^2 - 1 \right]}{\mu \left[\left(\frac{\mu_H}{\mu} \right)^2 - 1 \right]}. \quad (\text{D6})$$

It crosses eq. 6 at μ_C given by eq. D4, above which it is replaced by

$$n_{\text{max}}(\mu) = \frac{\mu}{\mu_H} n_H.$$

The n_{max} bound is also shown fig. 19 and appears in the upper regions. It suggests the maximally soft NS EOSs are incompatible with pQCD predictions with $X =$

1, and the problem starts early on at $n_{\chi\text{EFT}}$ where the first-order phase transitions take place. On one hand, identifying the earliest violation of eq. 12 is a strength of n_{max} . On the other hand, for an intuitive view of the non-perturbative effects required to satisfy eq. 12 (or equivalently the n_{max} bound), figs. 4 and 15 are better suited.

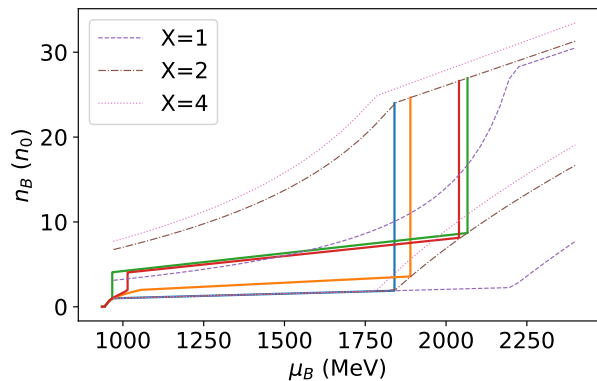


FIG. 19. The number density constraints imposed at $\mu_{\text{pQCD}} = 2.4$ GeV assuming $X = 1, 2, 4$ and at $\mu_L \approx 970$ MeV (the central value of χEFT prediction at n_0). The soft N3LO contribution is included. The colored solid curves are the modified maximally stiff and soft EOSs that are made to be compatible with eq. 17. The modification is described in the main text and starts at the critical points shown in fig. 6. They are obtained assuming the same set of pQCD parameters behind the underlying number density constraints. The critical points sit along the n_{min} bound, corroborating that the number density constraint is identical to eq. 17 applied at the critical points. For the number density constraint assuming $X = 1$, the maximally soft EOSs breach n_{max} which comes from ΔP_{min} , but as explained in section V A cannot be viewed as a constraint on the NS EOS.

Appendix E: Model-independent upper bound on Δ_{CFL}

Here, we report model-independent bounds on the highest Δ_{CFL} allowed by given NS maximum masses. Taking into account pairing contributions to the EOS eq. 13, the ΔP_{max} bound eq. 17 becomes

$$P_{\text{pQCD}} + P_{\text{CFL}} - P_{\text{TOV}} \leq \Delta P_{\text{max}} \quad (\text{E1})$$

from which we obtain

$$P_{\text{CFL}} \leq \Delta P_{\text{max}} - \Delta P. \quad (\text{E2})$$

For clarity, with the pairing effects included the quantities above are

$$\Delta P_{\text{max}} = \frac{n_{\text{CQM}} \mu_{\text{CQM}}}{2} \left[1 - \left(\frac{\mu_{\text{TOV}}}{\mu_{\text{CQM}}} \right)^2 \right]$$

and

$$\Delta P = P_{\text{pQCD}}(\mu_{\text{CQM}}) - P_{\text{TOV}}$$

where $\mu_{\text{CQM}} \equiv \mu_{\text{pQCD}} \equiv \mu_H$ is the baryon chemical potential at the chosen high-density matching point, n_{CQM} is given by eq. 13, and $P_{\text{pQCD}}(\mu_{\text{CQM}})$ is the perturbative contribution to the pressure.

For chosen pQCD EOS and the high-density matching point, the RHS of eq. E2 is a function of the TOV point and gives an upper bound $\max\{\Delta_{\text{CFL}}\}$ when the equality holds. It has a global maximum $\max\{\Delta_{\text{CFL}}\}$ across all NS EOSs reached by the maximally soft NS inner core EOSs. This is because the maximally soft NS EOSs predict the highest P_{TOV} at the highest μ_{TOV} . Large Δ_{CFL} yielding P_{CQM} too high for the maximally soft NS EOS will certainly overmatch other NS EOSs as well. We plot this upper bound along with sample-based statistics in fig. 20. The constraints strengthen rapidly with increasing X near $X \simeq 1$, largely due to the Δ_{CFL}^2 dependence in P_{CFL} . In the absence of additional assumptions, the CFL pairing gap at $\mu_B = 2.4$ GeV can be robustly placed below $\simeq 500$ MeV by the existence of two-solar-mass pulsars [55–59].

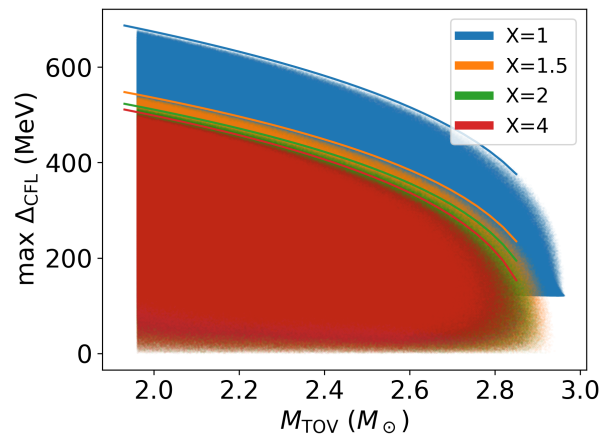


FIG. 20. Maximum allowed CFL pairing gaps as a function of M_{TOV} . The dots are computed for each EOS sample by solving Δ_{CFL} that saturates the inequality eq. E2. The lines are based on the maximally soft NS EOSs and give the global upper bound over all NS inner core EOSs. The partial N3LO pQCD contribution to the CQM EOS is included.

- [1] M. Troyer and U.-J. Wiese, Computational complexity and fundamental limitations to fermionic quantum Monte Carlo simulations, *Phys. Rev. Lett.* **94**, 170201 (2005), arXiv:cond-mat/0408370.
- [2] P. de Forcrand, Simulating QCD at finite density, *PoS LAT2009*, 010 (2009), arXiv:1005.0539 [hep-lat].
- [3] D. B. Kaplan, Chiral Symmetry and Lattice Fermions, in *Les Houches Summer School: Session 93: Modern perspectives in lattice QCD: Quantum field theory and high performance computing* (2009) arXiv:0912.2560 [hep-lat].
- [4] W. Baade and F. Zwicky, On super-novae, *Proceedings of the National Academy of Sciences* **20**, 254 (1934).
- [5] S. Weinberg, Nonlinear realizations of chiral symmetry, *Phys. Rev.* **166**, 1568 (1968).
- [6] S. Weinberg, Nuclear forces from chiral Lagrangians, *Phys. Lett. B* **251**, 288 (1990).
- [7] S. Weinberg, Effective chiral Lagrangians for nucleon - pion interactions and nuclear forces, *Nucl. Phys. B* **363**, 3 (1991).
- [8] S. Weinberg, Three body interactions among nucleons and pions, *Phys. Lett. B* **295**, 114 (1992), arXiv:hep-ph/9209257.
- [9] D. B. Kaplan, M. J. Savage, and M. B. Wise, Nucleon - nucleon scattering from effective field theory, *Nucl. Phys. B* **478**, 629 (1996), arXiv:nucl-th/9605002.
- [10] D. B. Kaplan, M. J. Savage, and M. B. Wise, A New expansion for nucleon-nucleon interactions, *Phys. Lett. B* **424**, 390 (1998), arXiv:nucl-th/9801034.
- [11] D. B. Kaplan, M. J. Savage, and M. B. Wise, Two nucleon systems from effective field theory, *Nucl. Phys. B* **534**, 329 (1998), arXiv:nucl-th/9802075.
- [12] S. R. Beane, P. F. Bedaque, M. J. Savage, and U. van Kolck, Towards a perturbative theory of nuclear forces, *Nucl. Phys. A* **700**, 377 (2002), arXiv:nucl-th/0104030.
- [13] T. Krüger, I. Tews, K. Hebeler, and A. Schwenk, Neutron matter from chiral effective field theory interactions, *Phys. Rev. C* **88**, 025802 (2013), arXiv:1304.2212 [nucl-th].
- [14] G. Wlazłowski, J. W. Holt, S. Moroz, A. Bulgac, and K. J. Roche, Auxiliary-field quantum Monte Carlo simulations of neutron matter in chiral effective field theory, *Phys. Rev. Lett.* **113**, 182503 (2014), arXiv:1403.3753.
- [15] S. Gandolfi, A. Lovato, J. Carlson, and K. E. Schmidt, From the lightest nuclei to the equation of state of asymmetric nuclear matter with realistic nuclear interactions, *Phys. Rev. C* **90**, 061306 (2014), arXiv:1406.3388 [nucl-th].
- [16] J. E. Lynn, I. Tews, J. Carlson, S. Gandolfi, A. Gezerlis, K. E. Schmidt, and A. Schwenk, Chiral three-nucleon interactions in light nuclei, neutron- α scattering, and neutron matter (2015), arXiv:1509.03470.
- [17] C. Drischler, K. Hebeler, and A. Schwenk, Chiral interactions up to next-to-next-to-next-to-leading order and nuclear saturation, *Phys. Rev. Lett.* **122**, 042501 (2019), arXiv:1710.08220 [nucl-th].
- [18] C. Drischler, J. A. Melendez, R. J. Furnstahl, and D. R. Phillips, Quantifying uncertainties and correlations in the nuclear-matter equation of state, *Phys. Rev. C* **102**, 054315 (2020), arXiv:2004.07805 [nucl-th].
- [19] B. A. Freedman and L. D. McLerran, Fermions and Gauge Vector Mesons at Finite Temperature and Density. 1. Formal Techniques, *Phys. Rev. D* **16**, 1130 (1977).
- [20] B. A. Freedman and L. D. McLerran, Fermions and Gauge Vector Mesons at Finite Temperature and Density. 3. The Ground State Energy of a Relativistic Quark Gas, *Phys. Rev. D* **16**, 1169 (1977).
- [21] C. Manuel, Hard dense loops in a cold nonAbelian plasma, *Phys. Rev. D* **53**, 5866 (1996), arXiv:hep-ph/9512365.
- [22] A. Kurkela, P. Romatschke, and A. Vuorinen, Cold Quark Matter, *Phys. Rev. D* **81**, 105021 (2010), arXiv:0912.1856 [hep-ph].
- [23] T. Gorda, A. Kurkela, R. Paatelainen, S. Säppi, and A. Vuorinen, Cold quark matter at N³LO: Soft contributions, *Phys. Rev. D* **104**, 074015 (2021), arXiv:2103.07427 [hep-ph].
- [24] A. Kurkela and A. Vuorinen, Cool quark matter, *Phys. Rev. Lett.* **117**, 042501 (2016), arXiv:1603.00750 [hep-ph].
- [25] T. Gorda, A. Kurkela, P. Romatschke, S. Säppi, and A. Vuorinen, Next-to-Next-to-Next-to-Leading Order Pressure of Cold Quark Matter: Leading Logarithm, *Phys. Rev. Lett.* **121**, 202701 (2018), arXiv:1807.04120 [hep-ph].
- [26] O. Komoltsev and A. Kurkela, How Perturbative QCD Constrains the Equation of State at Neutron-Star Densities, *Phys. Rev. Lett.* **128**, 202701 (2022), arXiv:2111.05350 [nucl-th].
- [27] T. Gorda, O. Komoltsev, and A. Kurkela, Ab-initio QCD Calculations Impact the Inference of the Neutron-star-matter Equation of State, *Astrophys. J.* **950**, 107 (2023), arXiv:2204.11877 [nucl-th].
- [28] R. Somasundaram, I. Tews, and J. Margueron, Perturbative QCD and the neutron star equation of state, *Phys. Rev. C* **107**, L052801 (2023), arXiv:2204.14039 [nucl-th].
- [29] C. E. Rhoades, Jr. and R. Ruffini, Maximum mass of a neutron star, *Phys. Rev. Lett.* **32**, 324 (1974).
- [30] S. Koranda, N. Stergioulas, and J. L. Friedman, Upper limit set by causality on the rotation and mass of uniformly rotating relativistic stars, *Astrophys. J.* **488**, 799 (1997), arXiv:astro-ph/9608179.
- [31] J. M. Lattimer and M. Prakash, Neutron star structure and the equation of state, *Astrophys. J.* **550**, 426 (2001), arXiv:astro-ph/0002232.
- [32] C. Drischler, S. Han, J. M. Lattimer, M. Prakash, S. Reddy, and T. Zhao, Limiting masses and radii of neutron stars and their implications, *Phys. Rev. C* **103**, 045808 (2021), arXiv:2009.06441 [nucl-th].
- [33] D. Zhou, On the parameterization of neutron star equations of state, in preparation (2023).
- [34] J. A. Melendez, R. J. Furnstahl, D. R. Phillips, M. T. Pratala, and S. Wesolowski, Quantifying Correlated Truncation Errors in Effective Field Theory, *Phys. Rev. C* **100**, 044001 (2019), arXiv:1904.10581 [nucl-th].
- [35] M. M. Forbes, S. Bose, S. Reddy, D. Zhou, A. Mukherjee, and S. De, Constraining the neutron-matter equation of state with gravitational waves, *Phys. Rev. D* **100**, 083010 (2019), arXiv:1904.04233 [astro-ph.HE].
- [36] D. Adhikari *et al.* (PREX), Accurate Determination of the Neutron Skin Thickness of ²⁰⁸Pb through Parity-Violation in Electron Scattering, *Phys. Rev. Lett.* **126**, 172502 (2021), arXiv:2102.10767 [nucl-ex].

- [37] B. T. Reed, F. J. Fattoyev, C. J. Horowitz, and J. Piekarowicz, Implications of PREX-2 on the Equation of State of Neutron-Rich Matter, *Phys. Rev. Lett.* **126**, 172503 (2021), arXiv:2101.03193 [nucl-th].
- [38] D. McKeen, A. E. Nelson, S. Reddy, and D. Zhou, Neutron stars exclude light dark baryons, *Phys. Rev. Lett.* **121**, 061802 (2018), arXiv:1802.08244 [hep-ph].
- [39] I. Tews, J. Carlson, S. Gandolfi, and S. Reddy, Constraining the speed of sound inside neutron stars with chiral effective field theory interactions and observations, (2018), arXiv:1801.01923 [nucl-th].
- [40] P. Landry and R. Essick, Nonparametric inference of the neutron star equation of state from gravitational wave observations, *Phys. Rev. D* **99**, 084049 (2019), arXiv:1811.12529 [gr-qc].
- [41] E. Annala, T. Gorda, A. Kurkela, J. Nättilä, and A. Vuorinen, Evidence for quark-matter cores in massive neutron stars, *Nature Phys.* **16**, 907 (2020), arXiv:1903.09121 [astro-ph.HE].
- [42] A. Vuorinen, The Pressure of QCD at finite temperatures and chemical potentials, *Phys. Rev. D* **68**, 054017 (2003), arXiv:hep-ph/0305183.
- [43] A. Ipp and A. Rebhan, Thermodynamics of large $N(f)$ QCD at finite chemical potential, *JHEP* **06**, 032, arXiv:hep-ph/0305030.
- [44] A. Deur, S. J. Brodsky, and G. F. de Teramond, The QCD Running Coupling, *Nucl. Phys.* **90**, 1 (2016), arXiv:1604.08082 [hep-ph].
- [45] T. Gorda, A. Kurkela, R. Paatelainen, S. Säppi, and A. Vuorinen, Soft Interactions in Cold Quark Matter, *Phys. Rev. Lett.* **127**, 162003 (2021), arXiv:2103.05658 [hep-ph].
- [46] T. Gorda, R. Paatelainen, S. Säppi, and K. Seppänen, Equation of State of Cold Quark Matter to $O(\alpha_s^3 \ln \alpha_s)$, *Phys. Rev. Lett.* **131**, 181902 (2023), arXiv:2307.08734 [hep-ph].
- [47] J. Frenkel and J. C. Taylor, High Temperature Limit of Thermal QCD, *Nucl. Phys. B* **334**, 199 (1990).
- [48] E. Braaten and R. D. Pisarski, Soft Amplitudes in Hot Gauge Theories: A General Analysis, *Nucl. Phys. B* **337**, 569 (1990).
- [49] J. C. Taylor and S. M. H. Wong, The Effective Action of Hard Thermal Loops in QCD, *Nucl. Phys. B* **346**, 115 (1990).
- [50] T. Gorda, A. Kurkela, J. Österman, R. Paatelainen, S. Säppi, P. Schicho, K. Seppänen, and A. Vuorinen, Degenerate fermionic matter at N3LO: Quantum electrodynamics, *Phys. Rev. D* **107**, L031501 (2023), arXiv:2204.11893 [hep-ph].
- [51] E. Braaten and A. Nieto, Free energy of QCD at high temperature, *Phys. Rev. D* **53**, 3421 (1996), arXiv:hep-ph/9510408.
- [52] E. Braaten and A. Nieto, Effective field theory approach to high temperature thermodynamics, *Phys. Rev. D* **51**, 6990 (1995), arXiv:hep-ph/9501375.
- [53] J. R. Oppenheimer and G. M. Volkoff, On Massive neutron cores, *Phys. Rev.* **55**, 374 (1939).
- [54] R. C. Tolman, Static solutions of Einstein's field equations for spheres of fluid, *Phys. Rev.* **55**, 364 (1939).
- [55] P. Demorest, T. Pennucci, S. Ransom, M. Roberts, and J. Hessels, Shapiro Delay Measurement of A Two Solar Mass Neutron Star, *Nature* **467**, 1081 (2010), arXiv:1010.5788 [astro-ph.HE].
- [56] J. Antoniadis *et al.*, A Massive Pulsar in a Compact Relativistic Binary, *Science* **340**, 6131 (2013), arXiv:1304.6875 [astro-ph.HE].
- [57] H. T. Cromartie *et al.* (NANOGrav), Relativistic Shapiro delay measurements of an extremely massive millisecond pulsar, *Nature Astron.* **4**, 72 (2019), arXiv:1904.06759 [astro-ph.HE].
- [58] R. W. Romani, D. Kandel, A. V. Filippenko, T. G. Brink, and W. Zheng, PSR J1810+1744: Companion Darkening and a Precise High Neutron Star Mass, *Astrophys. J. Lett.* **908**, L46 (2021), arXiv:2101.09822 [astro-ph.HE].
- [59] E. Fonseca *et al.*, Refined Mass and Geometric Measurements of the High-mass PSR J0740+6620, *Astrophys. J. Lett.* **915**, L12 (2021), arXiv:2104.00880 [astro-ph.HE].
- [60] C. Drischler, S. Han, and S. Reddy, Large and massive neutron stars: Implications for the sound speed within QCD of dense matter, *Phys. Rev. C* **105**, 035808 (2022), arXiv:2110.14896 [nucl-th].
- [61] M. G. Alford, K. Rajagopal, and F. Wilczek, QCD at finite baryon density: Nucleon droplets and color superconductivity, *Phys. Lett. B* **422**, 247 (1998), arXiv:hep-ph/9711395.
- [62] D. T. Son, Superconductivity by long range color magnetic interaction in high density quark matter, *Phys. Rev. D* **59**, 094019 (1999), arXiv:hep-ph/9812287.
- [63] M. G. Alford, K. Rajagopal, and F. Wilczek, Color flavor locking and chiral symmetry breaking in high density QCD, *Nucl. Phys. B* **537**, 443 (1999), arXiv:hep-ph/9804403.
- [64] T. Schäfer and F. Wilczek, Superconductivity from perturbative one gluon exchange in high density quark matter, *Phys. Rev. D* **60**, 114033 (1999), arXiv:hep-ph/9906512.
- [65] K. Rajagopal and F. Wilczek, The Condensed matter physics of QCD, in *At the frontier of particle physics. Handbook of QCD. Vol. 1-3*, edited by M. Shifman and B. Ioffe (2000) pp. 2061–2151, arXiv:hep-ph/0011333.
- [66] M. G. Alford, A. Schmitt, K. Rajagopal, and T. Schäfer, Color superconductivity in dense quark matter, *Rev. Mod. Phys.* **80**, 1455 (2008), arXiv:0709.4635 [hep-ph].
- [67] J. Berges and K. Rajagopal, Color superconductivity and chiral symmetry restoration at nonzero baryon density and temperature, *Nucl. Phys. B* **538**, 215 (1999), arXiv:hep-ph/9804233.
- [68] G. W. Carter and D. Diakonov, Light quarks in the instanton vacuum at finite baryon density, *Phys. Rev. D* **60**, 016004 (1999), arXiv:hep-ph/9812445.
- [69] R. D. Pisarski and D. H. Rischke, Gaps and critical temperature for color superconductivity, *Phys. Rev. D* **61**, 051501 (2000), arXiv:nucl-th/9907041.
- [70] J. Braun and B. Schallmo, From quarks and gluons to color superconductivity at supranuclear densities, *Phys. Rev. D* **105**, 036003 (2022), arXiv:2106.04198 [hep-ph].
- [71] D. Zhou, Dwarf (Twin) Neutron Stars I: Did GW170817 Involve One?, (2023), arXiv:2307.13810 [astro-ph.HE].
- [72] M. Alford, M. Braby, M. W. Paris, and S. Reddy, Hybrid stars that masquerade as neutron stars, *Astrophys. J.* **629**, 969 (2005), arXiv:nucl-th/0411016.
- [73] A. Kurkela, K. Rajagopal, and R. Steinhorst, Astrophysical Equation-of-State Constraints on the Color-Superconducting Gap, (2024), arXiv:2401.16253 [astro-ph.HE].
- [74] P. A. Baikov, K. G. Chetyrkin, and J. H. Kühn, Five-Loop Running of the QCD coupling constant, *Phys. Rev.*

- Lett. **118**, 082002 (2017), arXiv:1606.08659 [hep-ph].
- [75] R. L. Workman *et al.* (Particle Data Group), Review of Particle Physics, PTEP **2022**, 083C01 (2022).
- [76] A. Bazavov, N. Brambilla, X. G. Tormo, I. P. Petreczky, J. Soto, and A. Vairo, Determination of α_s from the QCD static energy: An update, Phys. Rev. D **90**, 074038 (2014), [Erratum: Phys.Rev.D 101, 119902 (2020)], arXiv:1407.8437 [hep-ph].
- [77] B. P. Abbott *et al.* (LIGO Scientific, Virgo), GW170817: Measurements of neutron star radii and equation of state, Phys. Rev. Lett. **121**, 161101 (2018), arXiv:1805.11581 [gr-qc].
- [78] S. De, D. Finstad, J. M. Lattimer, D. A. Brown, E. Berger, and C. M. Biwer, Constraining the nuclear equation of state with GW170817, Phys. Rev. Lett. **121**, 091102 (2018), arXiv:1804.08583 [astro-ph.HE].
- [79] C. D. Capano, I. Tews, S. M. Brown, B. Margalit, S. De, S. Kumar, D. A. Brown, B. Krishnan, and S. Reddy, Stringent constraints on neutron-star radii from multi-messenger observations and nuclear theory, Nature Astron. **4**, 625 (2020), arXiv:1908.10352 [astro-ph.HE].
- [80] B. Margalit and B. D. Metzger, Constraining the Maximum Mass of Neutron Stars From Multi-Messenger Observations of GW170817, Astrophys. J. **850**, L19 (2017), arXiv:1710.05938 [astro-ph.HE].
- [81] M. Shibata, E. Zhou, K. Kiuchi, and S. Fujibayashi, Constraint on the maximum mass of neutron stars using GW170817 event, Phys. Rev. D **100**, 023015 (2019), arXiv:1905.03656 [astro-ph.HE].